Retrieval of Raindrop Size Distribution, Vertical Air Velocity and Water Vapor Attenuation Using Dual-Wavelength Doppler Radar Observations

Lin Tian[1], Gerald M. Heymsfield[2], Lihua Li[1], and Ramesh C. Srivastava[3]

[1]*Goddard Earth Science and Technology Center, University of Maryland, Baltimore, Maryland*

[2]*NASA Goddard Space Flight Center, Greenbelt, Maryland*

[3]*Department of the Geophysical Sciences, The University of Chicago, Chicago, Illinois*

March 4, 2005
Submitted to the Journal of Applied Meteorology

Corresponding author's address: Lin Tian, NASA Goddard Space Flight Center, Code 613.1, Building 33, Rm C416, Greenbelt, MD 20771.
Email: tian@agnes.gsfc.nasa.gov

Abstract

Two techniques for retrieving the slope and intercept parameters of an assumed exponential raindrop size distribution (RSD), vertical air velocity, and attenuation by precipitation and water vapor in light stratiform rain using observations by airborne, nadir looking dual-wavelength (X-band, 3.2 *cm* and W-band, 3.2 *mm*) radars are presented. In both techniques, the slope parameter of the RSD and the vertical air velocity are retrieved using only the mean Doppler velocities at the two wavelengths. In the first method, the intercept of the RSD is estimated from the observed reflectivity at the longer wavelength assuming no attenuation at that wavelength. The attenuation of the shorter wavelength radiation by precipitation and water vapor are retrieved using the observed reflectivity at the shorter wavelength. In the second technique, it is assumed that the longer wavelength suffers attenuation only in the melting band. Then, assuming a distribution of water vapor, the melting band attenuation at both wavelengths and the rain attenuation at the shorter wavelength are retrieved. Results of the retrievals are discussed and several physically meaningful results are presented.

Popular Summary for "**Retrieval of Raindrop Size Distribution, Vertical Air Velocity and Water Vapor Attenuation Using Dual-Wavelength Doppler Radar Observations**" by Lin Tian, Gerald M. Heymsfield, Lihua Li, and Ramesh C. Srivastava submitted to Journal of Applied Meteorology.

Measuring global rainfall property by satellite such as Tropical Rain Measuring Mission (TRMM) is important for understanding weather and how to improve the weather predication. Rain has been very difficult to measure accurately over a wide range of intensities because there is generally insufficient information about the rain properties. A dual-wavelength radar, such as the one proposed for the Global Precipitation Measurement (GPM) can improve the accuracy of rainfall estimation. However, the 14 and 35 GHZ frequencies proposed for the GPM radar may not resolve the raindrop size distribution in light rain due to the small difference of the reflectivity at the two frequencies. By using combination of 94 GHz and 10 GHz reflectivity, and Doppler information that is not available on GPM, it has been found in this paper that light rain can be estimated more accurately.

A method is developed for estimating rainfall rate and other parameters in light stratiform rain using airborne Doppler radar observations at 94 and 10 GHz. The method uses the difference of the return power as well as Doppler velocity measured at the two frequencies to estimate rainfall rate, vertical air velocity, and water vapor attenuation that is nearly proportional to the water vapor content. The magnitudes and vertical variation of the averaged velocity are remarkably similar to what has been reported in the literature for area-averaged vertical velocity in extensive stratiform rain. The averaged profile of rainfall rate, and raindrop size distribution has shown evidence of drop breakup below the melting band and evaporation in the lower levels in the region of downdrafts. The potential ability to retrieve raindrop size distribution, vertical air velocity, and water vapor distribution as functions of the height is exciting because it offers the possibility of direct calculation of profiles of evaporation and, therefore, latent heating and cooling in the atmosphere using microphysical principles.

1. Introduction

Over the past several years, the Tropical Rainfall Measuring Mission (TRMM) has provided data for understanding storm formation and structure and improving weather prediction. Measurements by the single wavelength TRMM precipitation radar (PR) have been used to estimate profiles of attenuation–corrected reflectivity and rainfall rate (RR) (Iguchi et al. 2000). The data have also been used in conjunction with numerical cloud models to estimate latent heating / cooling.

The retrieval of RR by the TRMM PR and other single wavelength radars, is crucially dependent on the raindrop size distribution (RSD). Uncertainties in RSD are an inherent source of error in estimated RR. If the RSD depended on a single parameter, then the reflectivity (Z) at a single non-attenuating wavelength would suffice for retrieving RR. A commonly used one-parameter RSD is the Marshall-Palmer (MP) distribution (1948):

$$N(D) = N_0 \exp(-\Lambda D) \qquad (1.1).$$

Here $N(D)$ is the concentration of drops of diameter D per unit diameter interval, N_0 is a fixed intercept ($= 8 \times 10^{-2} \mathrm{cm}^{-4}$) and Λ, the slope of the distribution, is the sole variable parameter. Marshall and Palmer proposed the exponential distribution based on ground measurements of RSD in temperate latitudes. It has been widely used for the estimation of RR by radar. Subsequent measurements have confirmed the exponential form of the RSD, especially for stratiform rain, but have found the N_0 to be highly variable. For example, Waldvogel (1974) found that while the RSD is well represented by (1.1), N_0 ranges 2-3 orders of magnitude. This variability is a major source of error in estimation of RR by single-wavelength radar. Other measurements of RSD, especially in convective rain, have shown that it is more accurately described by the gamma distribution (Ulbrich 1983) which has three variable parameters. In this

paper, we shall confine ourselves to the two-parameter exponential RSD (1.1) with variable N_0 and Λ since we shall be concerned only with stratiform rain.

A dual-wavelength radar, such as the one proposed for the Global Precipitation Measurement (GPM) can provide RSD information and hence improve the accuracy of rainfall estimation. However, the 14 and 35 GHZ frequencies proposed for the GPM radar may not resolve the RSD in light rain due to the small difference of the reflectivity at the two frequencies. A combination of mm and cm wavelengths may provide more accurate information for light rain. Moreover, Doppler velocity, which improves the RSD estimation, as shown in this paper (see also, Meneghini et al. 2003), will not be available for the proposed GPM radar.

This paper presents techniques for estimating RSD and other parameters in light stratiform rain using Doppler radar observations at 3.2 cm and 3.2 mm wavelengths. In section 2, we present the basic radar equations. In section 3 we give a brief description of the radar observations used in this study. In sections 4 and 5, we present two techniques for retrieving the parameters of the RSD (1.1), the melting band attenuation, and water vapor attenuation and present the results obtained by application of the methods to the radar observations. Section 6 presents a summary and discussion of the work.

2. Basic Equations

This section presents the basic equations and introduces our notation and terminology. We neglect signal fluctuations, assume identical radar beams and simultaneous observations at the two wavelengths.

The received power, at range r, is expressed by the 'measured' equivalent radar reflectivity factor, $Z^{(m)}(r)$, or simply measured reflectivity; it is given by:

$$Z_{cm}^{(m)}(r) = Z_{cm}(r) \times A_{cm}(0,r) \qquad (2.1)$$

where $Z_{cm}(r)$ is the 'true' reflectivity and $A_{cm}(0,r)$ (≤ 1) is the attenuation factor, which accounts for losses due to the medium between the radar at $r=0$ and the range r. (A list of symbols and units is given in Appendix A.) In the above and subsequent equations, the subscripts *mm* and *cm* refer to the two wavelengths, 3.2 *mm* and 3.2 *cm* respectively, and the superscript (m) refers to measured quantities. The reflectivity that would be measured in the absence of attenuation, so-called 'true' reflectivity is given by:

$$Z_{cm} = c_Z \int_{D_{\min}}^{D_{\max}} N(D)\sigma_{BACK,cm}(D)dD \qquad (2.2)$$

where c_Z is a numerical unit conversion factor and $\sigma_{BACK}(D)$ is the back-scattering cross-section of drop of diameter D. The integral is taken from a minimum diameter $D_{\min}$ to a maximum diameter $D_{\max}$. Similar equations hold for the *mm* wavelength. The reflectivity is often expressed in *dBZ* units. We shall use ξ to represent Z in *dBZ* unit (we use corresponding Greek letters to express quantities in *dB* units). Equation (2.1) may be written as:

$$\xi_{cm}^{(m)}(r) = \xi_{cm}(r) - \alpha_{cm}(0,r) \qquad (2.3),$$

where

$$\xi_{cm} = 10\log_{10}(Z_{cm}),\ \xi_{cm}^{(m)} = 10\log_{10}\left(Z_{cm}^{(m)}\right) \qquad (2.4),$$

and

$$\alpha_{cm}(0,r) = -10\log_{10}\left[A_{cm}(0,r)\right] \qquad (2.5).$$

Here $\alpha_{cm}(0,r)$ is the two-way attenuation in dB between the radar and the range r. We decompose the attenuation factor into losses due to gases and precipitation and express it in terms of specific attenuation:

$$A(0,r) = A^{(gas)}(0,r) \times A^{(ppt)}(0,r) = \exp\left\{-\int_0^r \left[k^{(gas)}(r') + k^{(ppt)}(r')\right] dr'\right\} \qquad (2.6).$$

In the above, wavelength subscripts have been omitted and $k^{(gas)}$ and $k^{(ppt)}$ are the two-way specific attenuation coefficients due to gases and precipitation, respectively. We have not included attenuation by cloud water because we shall apply our method to stratiform *rain* with melting band and cloud water is not expected in the rain region. The two-way specific attenuation coefficient by rain is given by:

$$\kappa = c_k \int_{D_{\min}}^{D_{\max}} N(D)\sigma_{EXT}(D)dD \qquad (2.7),$$

where κ is k expressed in $dB / length$ units, $\sigma_{EXT}(D)$ is the extinction cross-section of drop of diameter D and c_k is a numerical unit conversion factor.

The measured mean Doppler velocity at the cm wavelength, $\bar{V}_{cm}^{(m)}$, is the reflectivity-weighted mean of the vertical velocity of the drops. It is given by:

$$\bar{V}_{cm}^{(m)} = \bar{V}_{cm} - w \qquad (2.8),$$

and

$$\bar{V}_{cm} = \frac{\int_{D_{\min}}^{D_{\max}} N(D)\sigma_{BACK,\,cm}(D)V_t(D)dD}{\int_{D_{\min}}^{D_{\max}} N(D)\sigma_{BACK,\,cm}(D)dD} \qquad (2.9).$$

where $\bar{V}$ is the reflectivity-weighted mean terminal fall speed, w is the vertical air velocity, and $V_t(D)$ is the terminal fall speed of drop of diameter D. The vertical air velocity is taken positive upwards, while the mean Doppler velocity and the terminal fall speed are taken positive downwards. Similar equations hold for the *mm* wavelength.

3. Observations

The observations used in this study were made in stratiform rain in the Florida area using nadir-looking airborne X-band (3.2 cm) and W-band (3.2 mm) Doppler radars. The aircraft flies at an altitude of 20 *km*. The range resolution for both wavelengths is 37.5 *m* and the beam-widths are 2.9°X2.9° and 0.6°X0.8° giving ground-footprints of approximately 1.0X1.0 and 0.21X0.28 km for the cm and mm wavelengths, respectively. The characteristics of the radars are summarized in Table 1. To minimize errors due to unmatched beams and signal fluctuations, the observations are averaged along the flight line. The Doppler velocity is corrected for aircraft motion and folding. Heymsfield et al. (1996) and Li et al. (2004) give detailed descriptions of the radars and data reduction procedures.

Figures 1 and 2 show the flight path and a nearby sounding. Figure 3 shows reflectivities and mean Doppler velocities for an extensive stratiform rain system with the top of the melting band at a height of about 4.3 km. The large decrease in reflectivity at the shorter wavelength with distance downwards below the melting band indicates severe attenuation by rain. Indeed, at distances less than about 135 *km* and greater than about 175 *km*, the $\xi_{mm}^{(m)}$ is below the radar

noise level near the surface. At the longer wavelength, we see a number of precipitation trails that can be followed from the ice into the rain region, and increases in the melting band reflectivity where the trails intersect the melting band. About eight trails can be identified at distances of about 121, 125, 132, 138-148, 150-156, 158-162, 163-165, 171 and 175 km; these distances refer to the points where the trails intersect the melting band. The trails can also be seen in the field of $\overline{V}_{cm}^{(m)}$. From the shapes of the trails, it is clear that the winds must be varying with height in both speed and direction. Unfortunately, sufficient nearby wind data were not available to perform calculations of trail shape. But it is clear that caution must be exercised in interpreting the vertical distributions of retrieved parameters in terms of column models of RSD evolution.

4. Retrieval I: Method and Results

Retrieval method I involves three steps. In the first step we use only the measured mean Doppler velocities to retrieve Λ, D_0 *and* w. In the second step we use an additional parameter, namely, $Z_{cm}^{(m)}$, to retrieve N_0. In the third and final step, we use $Z_{mm}^{(m)}$ to retrieve the distribution of water vapor attenuation. In the second and third steps, it is necessary to assume that there is no attenuation at the *cm* wavelength; however, the retrieval of Λ, D_0 *and* w in the first step is independent of attenuation at both wavelengths.

a. Step 1 – Retrieval of Λ, D_0 *and* w.

(i) Method

The mean Doppler velocities are independent of attenuation and N_0 and, moreover, their difference is independent of w:

$$\partial\bar{V}^{(m)} = \bar{V}_{cm}^{(m)} - \bar{V}_{mm}^{(m)} = \bar{V}_{cm} - \bar{V}_{mm} = \partial\bar{V} \qquad (4.1)$$

Thus, $\partial\bar{V}^{(m)}$ depends only on Λ. [We shall use ∂ as a dual-wavelength difference operator: $\partial(\ ) = (\ )_{cm} - (\ )_{mm}$.] The slope Λ and the median volume diameter, D_0 are related by:

$$\Lambda = 3.67/D_0 \qquad (4.2).$$

The above relation holds for RSD extending from zero to infinite diameter. For a truncated RSD, we regard D_0 as a proxy for Λ. Then, we have:

$$D_0 = f_V\left(\partial\bar{V}\right) \qquad (4.3)$$

where the function f_V depends only on $\partial\bar{V}$. Thus $\partial\bar{V}^{(m)}\left(=\partial\bar{V}\right)$ is sufficient for retrieving D_0 and Λ.

We have obtained f_V as follows. First, we calculated the back-scattering and extinction cross-sections for the two wavelengths, as a function of the drop diameter, using methods described in Mishchenko (2003). Calculations were done for horizontally oriented ellipsoidal drops. The drop shape was assumed as given by Pruppacher and Pitter (1971). The $D_{\min}$ and $D_{\max}$ were taken as 0.01 and 0.70 cm, respectively. Since the refractive index of water depends on the temperature, the calculations were done for 3 temperatures, namely, 5, 15, and 25 C, covering the range occurring in the observations. The refractive indices used in our calculations are given in Table 2. For the terminal fall speed, we used the analytical approximation given by Atlas et al. (1973) for an air density, ρ_0, near the ground. The terminal fall speed at a level having air density ρ is obtained by multiplying the ground-level value by $(\rho_0/\rho)^{0.4}$ (Foote and

duToit 1969). In practice, we reduced the observed Doppler velocities to the ground level by dividing it by the density factor. Finally, the integrals in equations (2.9) were evaluated numerically as a function of Λ.

Figure 4a (4b and 4c will be discussed later) shows plots of $\bar{V}_{cm}$, $\bar{V}_{mm}$ and $\partial\bar{V}$ against D_0 for a temperature of 15°C. We see that $\partial\bar{V}$ has a maximum at about $D_0 \cong 1.8\ mm$. At small D_0, $\partial\bar{V}$ is small because the scattering is in the Rayleigh regime at both the wavelengths; at large D_0, $\partial\bar{V}$ is small because of the saturation of terminal fall velocity with increasing drop size. Using this figure, we can calculate D_0 from observed $\partial\bar{V}^{(m)}$. One potential complication is that D_0 is a double-valued function of $\partial\bar{V}$. However, the peak of the $\partial\bar{V}$ curve occurs at about $\Lambda = 20\ cm^{-1}$. According to Marshall and Palmer (1948), $\Lambda = 20\ cm^{-1}$ corresponds to a rainfall rate of about $30\ mm\ hr^{-1}$. In stratiform rain, a rainfall rate exceeding $10\ mm\ hr^{-1}$ is very unlikely. Moreover, in our case, the *mm* wavelength radiation cannot penetrate any significant length of rain of this intensity. Therefore, in our case, D_0 will almost always be smaller than 1.8 mm and can be uniquely estimated from $\partial\bar{V}^{(m)}$. For practical use, it is efficient to use a polynomial fit between D_0 and $\partial\bar{V}$:

$$D_0 = \sum_{i=0}^{i=n} a_i \left(\partial\bar{V}\right)^i \qquad (4.4).$$

A third degree fit was found to give adequate accuracy. The fit is shown in Fig. 1a and the coefficients of the fit are given in Table 3. In estimating D_0, the fit for the temperature closest to the temperature at the observation height was used. Thus, if the RSD obeys (1.1), its Λ and D_0 can be retrieved from the measured differential mean Doppler velocity alone.

Once D_0 has been estimated, w can be retrieved simply as the difference between $\bar{V}_{cm}$ calculated from D_0 and the measured $\bar{V}_{cm}^{(m)}$ (equation 2.8). Our method of estimating w is superior to methods that use an analytically derived $Z-\bar{V}$ relationship (e.g., Rogers 1964) because such relationships assume a value of N_0 whereas our method does not.

(ii) Results

Figure 5 shows the measured $\xi_{cm}^{(m)}$ and $\partial\bar{V}^{(m)}$, and the retrieved D_0 and w fields. The D_0 field has trails similar to those in the fields of reflectivity and mean Doppler velocity. The general correspondence between the trails in the D_0 and $\xi_{cm}^{(m)}$ fields is noteworthy since $\xi_{cm}^{(m)}$ is not used in the retrieval of D_0. The w field also exhibits a trail structure similar to that in the $\xi_{cm}^{(m)}$ field. The updrafts and downdrafts do not appear to be always correlated with high or low reflectivities. This should not be surprising since w is a dynamic quantity which is affected by a number of factors including buoyancy and pressure perturbation forces. The general correspondence between the trail structures of the observed and retrieved parameters gives us confidence in the retrievals.

b. Retrieval of N_0 and R

(i) Method

So far we have used only the Doppler velocities. In this subsection, we use $Z_{cm}^{(m)}$ to retrieve the intercept N_0. For this purpose, we assume that there is no attenuation at the *cm* wavelength, that is

$$Z_{cm} = Z_{cm}^{(m)},\ \xi_{cm} = \xi_{cm}^{(m)} \tag{4.5}$$

This assumption is reasonable because the cm wavelength radiation suffers negligible attenuation by ice particles occurring in stratiform clouds (e.g., Battan, 1973). In the rain region, the attenuation is larger but still negligible. According to Battan, the two-way rain attenuation $\kappa_{cm} \cong .3,\ .08,\ .02\ dB\ km^{-1}$ for $R = 10,\ 3$ and 10 mm hr^{-1} respectively. Since in stratiform rain, R is generally less than a few mm hr^{-1}, we can neglect attenuation due to rain. Neglecting attenuation by particles in the melting region is more problematical. For now, we assume this attenuation to be also zero; this assumption will be reconsidered later. Now, from (2.2), (4.5) and (1.1), we have:

$$Z_{cm}^{(m)}/N_0 = Z_{cm}/N_0 = c_Z \int_{D_{\min}}^{D_{\max}} \exp(-\Lambda D)\sigma_{BACK,cm}(D)dD \qquad (4.6).$$

The right hand side of this equation is a function of Λ only. Therefore, this equation can be used to estimate N_0 from the measured $Z_{cm}^{(m)}$ and the already retrieved Λ. Once N_0 is known, integral parameters of the RSD such as R can be easily calculated.

(ii) Results

The retrieved N_0 and the calculated R are shown in Figs 6a and 6b. The trail structures in the fields of N_0 and R also have periodicity similar to that of the trails in the reflectivity field. Figure 7a shows a histogram of N_0. The N_0 values vary over more than two orders of magnitude and are generally less than the Marshall-Palmer value. Waldvogel (1974) reported observations of RSD in stratiform rain with a ground-based electromechanical raindrop spectrometer. His time series of N_0 (see, e.g. his Fig. 2) also show values of N_0 that are generally less than the Marshall-Palmer value. Uijlenhoet et al. (2003) reported disdrometer observations of RSD for a squall line. For an exponential fit to the RSD, they found values of

N_0 smaller than the M-P value in the transition and stratiform regions of the storm. In particular, in the stratiform portion of the rain, their N_0 is generally less than $3\times10^{-2}cm^{-4}$ which is the mode value in our histogram plot of N_0. Figure 7b shows a scatter plot of N_0 against $\xi_{cm}^{(m)}$. There is wide scatter in the values of N_0 but it shows a tendency to increase with $\xi_{cm}^{(m)}$ for $\xi_{cm}^{(m)}$ less than $25\ dBZ$. For higher reflectivities, the trend appears to be reversed. This is discussed further below. Figure 7c shows a plot of N_0, D_0, w and $\xi_{cm}^{(m)}$ against horizontal distance for four selected heights. At all four heights, peaks and troughs in N_0 are strongly correlated with troughs and peaks respectively in D_0. Similarly, peaks and troughs in $\xi_{cm}^{(m)}$ are fairly well correlated with peaks and troughs in D_0, especially for reflectivities smaller than about $25\ dBZ$. We do not have in-situ observations to support or refute these correlations. However, time series of $\Lambda(=3.67/D_0)$, N_0 and R in Figs. 2, 4 and 6 of Waldvogel (1974) also show strong correlations similar to those in our plots. A similar correlation is evident in the observations of Uijlenhoet et al. (see their Fig. 5), especially in the transition region of the precipitation. Such agreement with ground-based observations supports our retrievals. The similarity of correlations in the ground-observed and radar-retrieved parameters is remarkable considering the great disparity in the sample sizes in the two cases. Peaks and troughs in D_0 and w also generally occur together although the correlation is not as tight as in the cases of N_0 and D_0. Figure 7d shows a scatter plot of $\xi_{cm}^{(m)}$ vs. R together with regression equations reported in the literature and a best fit to the data. There is fair agreement between the slopes of the various regression equations. Our best-fit regression is higher than all the other regressions. We see that the increase of R with Z tends to slow down at about $25\ dBZ$. The scatter-plot of N_0 vs. Z (Fig. 7b) showed a similar change in trend at about $25\ dBZ$. One possible reason for this change in trends

in Figs. 7b and 7d may be the neglect of attenuation at the *cm* wavelength. It is possible that melting band attenuation become non-negligible at about 25 dBZ. In the next subsection, we shall see that the retrieved water vapor attenuation also supports this view.

c. Step 3 – Retrieval of Water Vapor Attenuation at the mm Wavelength

(i) Method

So far we have used the measured Doppler velocities and the reflectivity at the *cm* wavelength to retrieve N_0, D_0, w and integral parameters, assuming zero attenuation at the *cm* wavelength. We shall now use the $\xi_{mm}^{(m)}$ to retrieve attenuation suffered by the *mm* wavelength radiation.

The measured reflectivity at the *mm* wavelength is given by:

$$\xi_{mm}^{(m)}(r) = \xi_{mm}(r) - \alpha_{mm}^{(gas)}(0,r) - \alpha_{mm}^{(ppt)}(0,r_0) - \alpha_{mm}^{(ppt)}(r_0,r),\ r \geq r_0 \qquad (4.7),$$

where the attenuation is decomposed into that by gases and precipitation. At the *mm* wavelength, water vapor is responsible for almost all the gaseous absorption. The term $\alpha_{mm}^{(gas)}(0,r)$ represents the two-way integrated attenuation by water vapor from the radar to the range r, and $\alpha_{mm}^{(ppt)}(0,r_0)$ and $\alpha_{mm}^{(ppt)}(r_0,r)$ represent, respectively, the attenuations by precipitation particles from the radar to range r_0 and from range r_0 to the range r $(\geq r_0)$. We select the range r_0 $(\cong 3.8\ km)$ below the melting region where the ice particles have just melted into raindrops. Then, $\alpha_{mm}^{(ppt)}(0,r_0)$ stands for attenuation by particles in the ice and the melting regions. Applying (4.7) to range r_0:

$$\xi_{mm}(r_0) - \xi_{mm}^{(m)}(r_0) = \alpha_{mm}^{(gas)}(0, r_0) + \alpha_{mm}^{(ppt)}(0, r_0) \qquad (4.8).$$

Thus, the difference between the true and measured reflectivities at range r_0 is equal to the total integrated attenuation, at the *mm* wavelength, from the top of the cloud to range r_0 by water vapor and precipitation. The attenuation by water vapor at the colder temperatures at ranges less than r_0 is relatively small; for a saturated atmosphere, the two-way integrated attenuation from the top of the atmosphere down to 4 *km* height is about 1.5 *dB* (see Fig. 8c below). If we neglect the attenuation by the 'dry' ice particles above the melting band, then we can write:

$$\xi_{mm}(r_0) - \xi_{mm}^{(m)}(r_0) \cong \alpha_{mm,MB} \qquad (4.9)$$

where $\alpha_{mm,MB}$ represents the attenuation (dB), at the *mm* wavelength, by the melting band. In general, however, $\alpha_{mm,MB}$ should be interpreted as the total attenuation from the top of the cloud to the range r_0.

To use equations (4.7) – (4.9), we need the true reflectivity, ξ_{mm}. The true reflectivity can be calculated from the retrieved N_0 and Λ. However, we calculate it without making explicit use of the retrieved N_0. (This will facilitate the discussion of Retrieval Method II in the next section.) From (4.7) and (4.8), we have:

$$\left[\xi_{mm}(r) - \xi_{mm}^{(m)}(r)\right] - \left[\xi_{mm}(r_0) - \xi_{mm}^{(m)}(r_0)\right] = \alpha_{mm}^{(gas)}(r_0, r) + \alpha_{mm}^{(ppt)}(r_0, r),\ r \geq r_0 \quad (4.10).$$

Thus, the difference between the true and measured reflectivities at r and r_0 is equal to the sum of the integrated attenuations, between the two ranges, by gases and precipitation. We solve (4.10) for the gas attenuation:

$$\alpha_{mm}^{(gas)}(r_0,r)=\left[\xi_{mm}^{(m)}(r_0)-\xi_{mm}^{(m)}(r)\right]-\left\{\xi_{mm}(r_0)-\xi_{mm}(r)\right\}-\alpha_{mm}^{(ppt)}(r_0,r),\ r\geq r_0 \quad (4.11).$$

The term in the square brackets is observed. Again, the term in the curly brackets and the quantity $\alpha_{mm}^{(ppt)}(r_0,r)$ can be calculated using the retrieved N_0 and Λ. Again, we calculate them also without making explicit use of the retrieved N_0. We write the true reflectivity as:

$$\xi_{mm}=\xi_{cm}-\left(\xi_{cm}-\xi_{mm}\right)=\xi_{cm}-\partial\xi \quad (4.12)$$

The term $\partial\xi$ is independent of N_0 and is a function of Λ only. Further, since Λ is a function of $\partial\bar{V}$ alone, we can express $\partial\xi$ also as a function of $\partial\bar{V}$ alone:

$$\partial\xi=f_{\xi}\left(\partial\bar{V}\right) \quad (4.13)$$

We have evaluated this function numerically (Fig. 1b). In practice, it is efficient to use a polynomial fit:

$$\partial\xi=\sum_{i=0}^{i=n}b_i\left(\partial\bar{V}\right)^i \quad (4.14)$$

to calculate $\partial\xi$ from the observed $\partial\bar{V}^{(m)}=\partial\bar{V}$. This gives us the terms in the curly brackets of (4.11). The remaining term of (4.11) is evaluated as follows. We have:

$$\alpha_{mm}^{(ppt)}(r_0,r)=c_k\int_{r_0}^{r}\kappa_{mm}(r')dr' \quad (4.15).$$

Now from (1.1), (2.2) and (2.3):

$$\frac{\kappa_{mm}}{Z_{cm}}=\frac{c_{k,mm}\int_{D_{\min}}^{D_{\max}}\exp(-\Lambda D)\sigma_{EXT,mm}(D)dD}{c_{Z,cm}\int_{D_{\min}}^{D_{\max}}\exp(-\Lambda D)\sigma_{BACK,cm}(D)dD} \quad (4.16).$$

Thus κ_{mm}/Z_{cm} is independent of N_0 and is a function of Λ only. Therefore, it too can be expressed as a function of $\partial\bar{V}$:

$$\kappa_{mm}/Z_{cm} = f_{\kappa/Z}\left(\partial\bar{V}\right) \tag{4.17}$$

We again fit a polynomial to the function $f_{\kappa/Z}\left(\partial\bar{V}\right)$:

$$\kappa_{mm}/Z_{cm} = f_{\kappa/Z}\left(\partial\bar{V}\right) = \sum_{i=1}^{i=n} h_i\left(\partial\bar{V}\right)^i \tag{4.18}$$

Figure 1c shows a plot of $f_{\kappa/Z}\left(\partial\bar{V}\right)$ together with the polynomial fit. The coefficients of the fits are given in Table 3. Using (4.15) and (4.18), we have:

$$\alpha_{mm}^{(ppt)}(r_0,r) = c_k\int_{r_0}^{r} Z_{cm}(r')\left[\sum_{i=1}^{i=n} h_i\left[\partial\bar{V}(r')\right]^i\right]dr' \tag{4.19}$$

Thus, $\alpha_{mm}^{(ppt)}(r_0,r)$ can be calculated from the measured $Z_{cm}^{(m)} = Z_{cm}$ and $\partial\bar{V}^{(m)}$ $(=\partial\bar{V})$. Equation (4.11) then yields the integrated water vapor attenuation $\alpha_{mm}^{gas}(r_0,r)$. An estimate of specific attenuation by water vapor can be obtained by differentiating $\alpha_{mm}^{gas}(r_0,r)$. The specific attenuation can be translated into water vapor content using a temperature sounding and the known dependence of the specific attenuation on temperature, pressure and water vapor content (Ulaby et al. 1982).

(ii) Results

Figure 8a shows $\alpha_{mm,MB}$, the retrieved two-way attenuation at the *mm* wavelength by precipitation particles and the water vapor from the top of the cloud to just below the melting band, and $\xi_{cm,MB}$, the maximum $cm-$wavelength reflectivity in the melting band, as functions of the horizontal distance. Except for a small noisy region near 126 *km*, all the retrieved

attenuations are positive. Moreover, there is a strong correlation between the peaks and troughs of the two quantities lending further support to the retrieval.

The retrieved two-way integrated water vapor attenuation, $\alpha_{mm}^{gas}(r_0,r)$, between 135 & 170 *km* is shown in the Fig. 8b (the *mm*-wave signal is noisy in the other regions). First, we notice that the attenuation is highly variable. This means that the water vapor distribution must also be highly variable. We also see a trail structure in the integrated attenuation. This should not be surprising since the water vapor is affected by evaporation / condensation, which depends on the RSD and the vertical air velocity and these latter quantities have trail structures. Secondly, the total integrated attenuation occasionally exceeds that calculated for a saturated atmosphere ($7.2\ dB$). As argued later, this unphysical result may be due to our assumption of zero attenuation at the *cm* wavelength. Thirdly, the integrated attenuation sometimes decreases with distance downwards. This is also an unphysical result because the integrated attenuation should increase downwards monotonically. This is better seen in the vertical profiles for four selected horizontal distances (Fig. 9).

For each distance, Fig. 9 shows three sets of measured and retrieved quantities, namely, (left) $\xi_{cm}^{(m)}$, $\xi_{cm}^{(m)}$, ξ_{mm}, (middle) $\bar{V}_{cm}^{(m)}$, $\bar{V}_{mm}^{(m)}$, and (right) $\alpha_{mm}^{(gas)}$, $\alpha_{mm}^{(ppt)}$ and integrated gas attenuation computed for a saturated atmosphere from the sounding using equations in Ulaby et al. (1982). The following discussion applies mostly to the right panels.

At 138.5 *km*, the retrieved integrated water vapor attenuation $\alpha_{mm}^{(gas)}$ increases downwards monotonically except for small decreases at certain heights. These decreases may be due to signal fluctuations. Comparison of retrieved and computed attenuations suggests an unsaturated atmosphere with a relative humidity of about 50%. The integrated rain attenuation below r_0 is

about 6.5 dB. At 142 km also, $\alpha_{mm}^{(gas)}$ increases downward almost monotonically but there is a rather thick layer of supersaturated air below about1.5 km height. Again at 144 km, $\alpha_{mm}^{(gas)}$ has an almost monotonic profile except for a rather deep downward decreasing section just below r_0. This profile also has an unphysical shallow supersaturated column below about 0.5 km. The integrated rain attenuation below r_0 is about 4 dB. The supersaturated column may be due to an underestimate of attenuation by precipitation, which in turn may be due to the neglect of attenuation at the cm wavelength as discussed later. The profile of $\alpha_{mm}^{(gas)}$ at 152 km is the most anomalous. This anomaly is also quite evident in Fig. 8b. It probably involves a breakdown of our assumption of an exponential RSD. Because of the occasional non-monotonic nature of the retrieved integrated attenuation, we have not attempted to recover the distribution of water vapor.

5. Retrieval II: Method and Results

The first retrieval method gave us some physically meaningful results but we also noted certain deficiencies in the results: (a) the integrated water vapor attenuation occasionally decreased with distance downwards, (b) occasionally the water vapor attenuation implied supersaturated air, and (c) the plots of $\xi_{cm}^{(m)}$ vs. N_0 and $\xi_{cm}^{(m)}$ vs. R showed a change in trend at a reflectivity of about 25 dBZ. As regards (a), decreases of small magnitudes over a few range bins may be due to signal fluctuations but decreases of larger magnitudes over many range bins are problematic. The more significant anomalies may involve breakdown of the assumption of exponential RSD. Discrepancies (b) and (c) may be due, at least in part, to neglect of attenuation at the $cm-$wavelength. As pointed out earlier, neglect of attenuation by raindrops and ice particles is justifiable. However, attenuation by mixed phase and melting particles may start to become significant at about 25 dBZ. Bellon et al. (1997) reported melting band attenuation at3.2 $cm-$wavelength of about 0.5 dB (1.7 dB) for a rain reflectivity, below the melting band,

of $23\ dBZ$ ($36.5\ dBZ$). The Bellon et al. measurements were made in temperate-latitude precipitation, whereas the observations discussed here were made in tropical precipitation. For a given reflectivity, the melting band attenuation could be greater in tropical precipitation because larger, more deformed, mixed-phase particles which are responsible for the attenuation are more likely in tropical precipitation. Qualitatively, we can see the effect of non-zero melting band attenuation on the retrievals of the previous section. First, we note that the retrieved Λ, D_0 and w will remain unchanged because those retrievals are unaffected by attenuation. Second, with finite melting-band attenuation at the $cm-$wavelength, Z_{cm} would exceed $Z_{cm}^{(m)}$ for $r \geq r_0$. Consequently, N_0 retrieved assuming non-zero melting band attenuation would be greater than that deduced by Method I. Thus, with finite melting band attenuation, the retrieved RSD would have the same slope but a greater intercept than that retrieved by Method I. Because of the increased intercept, the estimated attenuation by precipitation would be greater, which would result in reduced values of the retrieved integrated water vapor attenuation. This may help to resolve problem (b) above. Also, it may be shown that neglect of melting band attenuation tends to produce the tendencies noted in (c) above.

Below, we present a method for retrieving the melting band attenuation at the $cm-$wavelength from the measurements. Results of application of this method are presented in subsection *b*. A synopsis and comparison of the results from methods I and II are presented in subsection *c*.

a. Method

To retrieve the melting band attenuation at the $cm-$wavelength, we need the profile of water vapor attenuation at the $mm-$wavelength; it can be calculated if the distribution of water vapor is known. For this purpose, we use the temperature sounding of Fig. 2 and assume a saturated atmosphere. However, the method can be applied to any given distribution of water vapor.

The first step is the retrieval of Λ, D_0 and w as in section 4a (i). Next, denoting the melting band attenuation at the $cm-$wavelength by $A_{cm,MB}$ ($\alpha_{cm,MB}$ dB), equation (4.5) gives:

$$Z_{cm} = Z_{cm}^{(m)}/A_{cm,MB},\ \xi_{cm} = \xi_{cm}^{(m)} + \alpha_{cm,MB},\ r > r_0 \tag{5.1}$$

Thus, for $r \geq r_0$, the true reflectivity (dBZ) at the $cm-$wavelength exceeds the measured reflectivity (dBZ) by a constant equal to the melting band attenuation in dB. The intercept of the RSD is given by the following equation (see equation 4.6):

$$N_0 = \left[Z_{cm}^{(m)}/A_{cm,MB}\right] \Big/ \left[c_Z \int_{D_{\min}}^{D_{\max}} \exp(-\Lambda D)\sigma_{BACK,cm}(D)dD\right] = \frac{N_0^*}{A_{cm,MB}} \tag{5.2}.$$

where N_0^* is the intercept under the assumption of zero melting band attenuation at the $cm-$wavelength. We see that $N_0 > N_0^*$.

The second step involves estimation of $A_{cm,MB}$. For this, we use the measured reflectivities at both wavelengths. From (4.7) and (5.1), we have:

$$\begin{aligned} \xi_{cm}^{(m)}(r) - \left[\xi_{mm}^{(m)}(r) + \alpha_{mm}^{(gas)}(0,r)\right] - \left\{\xi_{cm}(r) - \xi_{mm}(r)\right\} \\ = \alpha_{mm}^{(ppt)}(r_0,r) + \left[\alpha_{mm}^{(ppt)}(0,r_0) - \alpha_{cm,MB}\right],\ r \geq r_0 \end{aligned} \tag{5.3}$$

or

$$\partial\xi_p^{(m)}(r) - \partial\xi(r) = \left\{\alpha_{mm}^{(ppt)}(r_0,r) - \partial\alpha_{MB}\right\},\ r \geq r_0 \tag{5.4},$$

where

$$\partial\xi_p^{(m)}(r) \equiv \xi_{cm}^{(m)}(r) - \left[\xi_{mm}^{(m)}(r) + \alpha_{mm}^{(gas)}(0,r)\right] \tag{5.5},$$

$$\partial\xi(r) \equiv \left[\xi_{cm}(r) - \xi_{mm}(r)\right] \tag{5.6},$$

and

$$\partial\alpha_{MB} \equiv \alpha_{cm,MB} - \alpha_{mm}^{(ppt)}(0,r_0) \cong \alpha_{cm,MB} - \alpha_{mm,MB} \tag{5.7}.$$

The term, in square brackets on the left hand side of (5.3) is the *mm* wavelength reflectivity that would be observed in the absence of gas attenuation. Together, the first two terms on the left hand side thus represent the difference of the reflectivities at the two wavelengths due to precipitation alone. This quantity is denoted by the symbol $\partial\xi_p^{(m)}$ (Eq. 5.5). The last term on the left hand side of (5.3) is the difference of the true reflectivities at the two wavelengths and is denoted by $\partial\xi$ (Eq. 5.6); in the literature, it is often called the dual-wavelength ratio. The left hand side of (5.3) is thus the difference between the measured and true differential reflectivities. Then the right hand sides of (5.3) (and 5.4) are equal to the difference between the integrated attenuations from the radar to the range under consideration at the *mm* and *cm* wavelengths. This differential attenuation is split into attenuation between the radar and the range r_0 and between r_0 and $r\,(\geq r_0)$. The latter quantity is simply the rain attenuation at the *mm* wavelength between r_0 and r since we assume rain attenuation at the longer wavelength to be zero. At the longer wavelength, the only attenuation between the radar and r_0 is due to the melting band. If we assume that at the shorter wavelength also the attenuation is due to the melting band only then the former quantity is simply the differential melting band attenuation, equation (5.7). A special case of equation (5.3) occurs when the scattering at both wavelengths is in the Rayleigh regime and there is no attenuation at the longer wavelength. Then $\partial\xi$ equals zero, and the term in the curly brackets, in equation (5.4), is simply the integrated attenuation by precipitation at the shorter wavelength. These conditions are fairly well satisfied by radiation of wavelengths 10 and 3 *cm* (e.g. Eccles and Mueller 1971).

Now we consider application of equation (5.4) to the observations. The first term of this equation is given by observation and the assumed water vapor distribution. The second term can be evaluated from the observed $\partial\bar{V}$ using equation (4.13). This gives an estimate of the term in

the curly brackets in (5.4). Putting $r = r_0$ in this equation, we obtain an estimate of the differential melting band attenuation:

$$\partial\alpha_{MB} = \alpha_{cm,MB} - \alpha_{mm,MB} = \partial\xi(r_0) - \partial\xi^{(m)}(r_0) \qquad (5.8).$$

Once $\partial\alpha_{MB}$ is known, we can apply (5.4) to ranges $r > r_0$ to estimate the integrated attenuation by precipitation:

$$\begin{aligned}\alpha_{mm}^{(ppt)}(r_0,r) &= \partial\alpha_{MB} + \partial\xi_p^{(m)}(r) - \partial\xi(r) \\ &= \left[\partial\xi_p^{(m)}(r) - \partial\xi^{(m)}(r_0)\right] - \left[\partial\xi(r) - \partial\xi(r_0)\right]\end{aligned} \qquad (5.9).$$

It is noted that the above estimate of $\alpha_{mm}^{(ppt)}(r_0,r)$ involves the measured differential Doppler velocity, the measured reflectivities at *both* wavelengths and the assumed water vapor distribution. We can get a second estimate of $\alpha_{mm}^{(ppt)}(r_0,r)$ using only the measured differential Doppler velocity *and* the measured reflectivity at the $cm-$wavelength. Using (4.15), (4.17), and (5.1), we have:

$$\begin{aligned}\alpha_{mm}^{(ppt)}(r_0,r) &= c_\kappa \int_{r_0}^{r} \kappa_{mm}(r')dr' = \frac{c_\kappa}{A_{cm,MB}} \int_{r_0}^{r} \frac{\kappa_{mm}(r')}{Z_{cm}(r')} Z_{cm}^{(m)}(r')dr' \\ &= \frac{c_\kappa}{A_{cm,MB}} \int_{r_0}^{r} f_{\kappa/Z}\left(\partial\bar{V}(r')\right) Z_{cm}^{(m)}(r')dr' = \frac{\alpha_{mm}^{(ppt)*}(r_0,r)}{A_{cm,MB}}\end{aligned} \qquad (5.10).$$

In the above equation, $\alpha_{mm}^{(ppt)*}(r_0,r)$ represents the integrated attenuation by precipitation under the assumption of zero attenuation at the $cm-$wavelength. Equations (5.9) and (5.10) give two independent estimates of $\alpha_{mm}^{(ppt)}(r_0,r)$ which should be identical. This condition can be used to estimate $A_{cm,MB}$ and then $\alpha_{mm,MB}$ can be retrieved from $\partial\alpha_{MB}$ (Eq. 5.7). A method for retrieving these quantities is illustrated in the schematic of Fig. 10. The curve marked A represents $\partial\xi_p^{(m)}$. Since it involves the observed reflectivities, it is noisy. The curve marked B represents $\partial\xi$; it is calculated from the observed $\partial\bar{V}^{(m)}$ and, as such, it is also noisy. The difference of these two

curves is labeled C and equals $\alpha_{mm}^{(ppt)}(r_0,r)-\partial\alpha_{MB}$. At the height marked r_0, the displacement of this curve from the ordinate should equal $-\partial\alpha_{MB}$. However, we do not take this displacement as an estimate of $-\partial\alpha_{MB}$ because of the noisy nature of the curves. The curve labeled D represents $\alpha_{mm}^{(ppt)}*(r_0,r)$ and is obtained by evaluating the integral in the fourth member of equation (5.10) numerically. This curve turns out to be relatively smooth because it is the integral of a positive quantity. In practice, it is also found to be fairly linear. The curve D when divided by $A_{cm,MB}(<1)$ and displaced to the right by the amount $-\partial\alpha_{MB}$ should coincide with the curve C. Fitting techniques can be used to find the displacement and $A_{cm,MB}$ to achieve the best fit between curves D and C. However, in view of the rather questionable validity of the assumption of a saturated atmosphere, we use a simple linear least squares fitting technique. First, we smooth the curve C by making a linear least squares fit to it. The line labeled L shows the fitted line. A few range gates nearest to the ground are excluded from this fitting procedure because of possible ground contamination of those observations. The displacement of the fitted line from the ordinate at range r_0 is taken as an estimate of $-\partial\alpha_{MB}$ and the ratio of the slopes of the lines D and L gives an estimate of $A_{cm,MB}$.

b. Results from Retrieval Method II

Because of uncertainty regarding the distribution of water vapor, the following results should not be regarded as definitive but rather as illustrative of the retrieval method; our main purpose here is to develop a retrieval method that can be used if the water vapor distribution is known or measured independently.

Figures 11 shows profiles of the quantities in the schematic of Fig. 10 for the same four horizontal distances as in Fig. 9. The melting band attenuations at the *mm* wavelength (strictly, attenuation by gases and precipitation from the top of the cloud to the range r_0 obtained by

methods I and II are comparable. For method I, the values are 7.80, 4.18, 5.42, 6.42 dB while for method II they are 6.89, 5.54, 5.62, 5.40 dB. The retrieved melting band attenuations for the cm wavelength are: –0.46, 3.79, 3.07, $-4.91\ dB$. The negative attenuations are unphysical and the positive attenuations are higher than would be expected on the basis of Bellon et al.'s measurements. These discrepancies bring out the importance of the water vapor attenuation profile for the retrieval method. The ratio of the slopes of the best-fit line L and the line D gives $1/A_{cm,MB}$. For a positive melting band attenuation, this ratio should be greater than 1. In Fig. 11a, it is slightly less than 1, which yields a negative $\alpha_{cm,MB}$. The slope of the line L is determined by line C, which is obtained from the observed reflectivities and the assumed integrated gas attenuation. If we had assumed smaller gas attenuation, then the line C would be rotated counterclockwise and would have a greater slope, which would then have yielded a positive value for the melting band attenuation. In support of this, we see from Fig. 9a that Method I, which assumed zero melting band attenuation at the longer wavelength, gave an integrated gas attenuation about half that for a saturated atmosphere. In Figs. 11b and 11c the ratio of the slopes mentioned above is greater than unity and consequently the melting band attenuations are positive but rather large in magnitude. Again, an adjustment of the assumed water vapor distribution could alter these results in a more plausible direction. Figure 11d yields a result similar to that of Fig. 11a and is again probably due to an overestimate of water vapor attenuation.

c. Horizontally Averaged Results from Retrieval Methods I and II

In this subsection, we present profiles of horizontal averages of certain observed and retrieved quantities for the region $135-155\ km$. Only the region of $135-155\ km$ were used in the averaging because the received power, at the shorter wavelength, is near or below the noise

level in the other regions. Profiles that yielded negative melting band attenuation at the longer wavelength have also been ignored in this averaging.

Figure 12a shows the measured reflectivities for the two wavelengths and the retrieved 'true' reflectivity at the longer wavelength. The strong attenuation suffered by the *mm* wavelength is obvious. The measured and 'true' reflectivities, at the *cm* wavelength, differ by a constant amount equal to the average melting band attenuation for this wavelength deduced by Method II. This difference, about 2.5 *dB*, is rather large and is probably overestimated because of the assumption of a saturated atmosphere in Method II. The downward decrease of the reflectivity at the *cm* wavelength is probably due to evaporation and drop breakup. The total decrease of reflectivity from the top to the bottom of the column is about 5 *dB*.

Figure 12b shows measured mean Doppler velocities and the retrieved vertical air velocity. As mentioned earlier, the retrieved w is the same for both methods. There is an updraft above about 2.7 *km* and downdraft below. The peak upward velocity of about 25 cm s^{-1} occurs at the top of the column; the downdraft increases downwards reaching a maximum magnitude of about 25 cm s^{-1} at about 1 *km* above ground. Below 1 *km*, the downdraft shows a satisfactory decrease towards the ground. The pattern and magnitudes of the retrieved vertical air velocities are characteristic of extensive stratiform rain (e.g., Houze, 1993, Chapter 9; Srivastava et al, 1986). The studies in the literature have used VAD or other methods to infer area-averaged vertical air velocities. Here we have been able to deduce vertical velocities in stratiform rain from vertical incidence Doppler radar observations at two wavelengths.

Figure 12c shows the median volume diameter, D_0, and the intercept parameter, N_0. The D_0 is the same for both retrieval methods. The N_0 is greater for Method II. It increases rather rapidly from the top of the column to a height of about 2 *km* and is approximately

constant below that height. The D_0 also decreases rapidly down to a height of about 2 *km* and more slowly below that height. The rainfall rate deduced by both methods (Fig. 12d) is approximately constant from the top of the column down to a height of about 2 *km* but decreases below that height. The rainwater content (Fig. 12d) shows a small increase (Method II) from the top of the column to a height of about 2 *km* and decreases below that height. The decreases in N_0 and D_0 from the top of the column to about 2 *km* height are consistent with breakup of drops formed by the melting of large aggregate snowflakes. This is further supported by the near constancy of the rainfall rate in this height interval. For a fixed R, the decrease in D_0 implies an increase in the rainwater content. The constancy of N_0 and the slower decrease of D_0 below 2 *km* height are consistent with rain evaporation. This is also supported by the downward decrease of rainfall rate in this region. We also note that there is downdraft in the region where the rainfall rate and rainwater content are decreasing with distance downwards. The above deductions are physically reasonable and consistent but should be regarded as somewhat speculative because of the lack of independent supporting measurements. In future, additional measurements, perhaps at a third frequency, could be used to refine and extend the retrievals and further support the physical deductions.

Figure 12e shows profiles of integrated water vapor attenuation retrieved by Method I and that calculated for a saturated atmosphere. The averaged attenuation increases monotonically downwards and shows a nearly saturated or a somewhat supersaturated atmosphere. Individual profiles presented earlier sometimes showed sections having an unphysical decrease downwards or rather large supersaturations. These are not seen in the averaged profile. It is possible that the averaging has served to remove errors due to signal fluctuations and beam mismatch. The small supersaturation in the lower levels is probably due to the neglect of melting band attenuation in

Method I. Another possibility is that the sounding used to compute the attenuation may not be quite applicable to the region of the radar measurements.

6. Summary and Discussion

We have presented observations of light stratiform rain with melting band by airborne dual-wavelength, nadir-looking radars. The radars measure reflectivities and mean Doppler velocities at two wavelengths - 3.2 *cm* and 3.2 *mm*. Except for very large raindrops, the scattering at the longer wavelength is in the Rayleigh regime; at the shorter wavelength it is in the Mie regime except for the very smallest raindrops. There is also strong attenuation at the shorter wavelength. Consequently, the mean Doppler velocities and reflectivities measured at the two wavelengths are different. These differences have been exploited to retrieve RSD parameters, water vapor and precipitation attenuation, melting band attenuation and vertical air velocity. Two retrieval methods have been presented. In both methods, we assume the RSD to be exponential with two free parameters - slope, Λ, and intercept, N_0. In both methods, the Λ (equivalently D_0) and the vertical air velocity have been estimated from the mean Doppler velocities alone. In Method I, the N_0 has been retrieved from the measured reflectivity at the longer wavelength assuming no attenuation at this wavelength. From the retrieved Λ and N_0, integral parameters of the RSD such as rainwater content and rainfall rate have been calculated. Additionally, in Method I, the measured reflectivity at the shorter wavelength has been used to retrieve attenuation at this wavelength by the melting band and the water vapor below it. We believe that this is the first time that range-resolved attenuation by water vapor has been retrieved by active radar in a precipitating situation. In retrieval method II, we dropped the assumption of zero attenuation at the longer wavelength to the extent of assuming a finite melting band attenuation. Under the further assumption of a known distribution of water vapor, we have presented a method for retrieving the melting band attenuations at both wavelengths and

the rain attenuation at the shorter wavelength. For illustration, Method II has been applied assuming a saturated atmosphere.

Lacking independent in-situ and / or ground based measurements, we have argued in favor of the validity of our retrievals on the basis of physical plausibility and consistency. The retrieved parameters such as D_0, Λ, and the vertical air velocity have trail structures similar to those of observed reflectivity and mean Doppler velocity at the longer wavelength. A strong negative correlation found between the peaks and troughs of retrieved D_0 and N_0 is similar to that reported in ground-based observations in stratiform precipitation by others. The numerical values and scatter of the retrieved N_0 are also similar to those found in ground-based studies of stratiform rain RSD. The retrieved melting band attenuation at the shorter wavelength has shown strong positive correlation with melting band reflectivity at the longer wavelength. The profiles of the integrated water vapor attenuation retrieved by Method I have been found to be generally increasing with distance downwards as would be expected. The profiles generally implied a sub-saturated atmosphere as is physically plausible for extensive stratiform rain. Small increases of the retrieved integrated water vapor attenuation with distance downwards have been attributed to signal fluctuations, while larger anomalies have been attributed to breakdown of the assumption of exponential RSD. Some supersaturated regions have also been indicated by the retrievals, especially in the lower levels. These have been attributed to the neglect of attenuation at the longer wavelength. Accordingly, in retrieval Method II, we dropped the assumption of zero melting band attenuation at the longer wavelength. Application of Method II requires knowledge of the distribution of water vapor. The illustrative retrievals in section 5 assumed a saturated atmosphere. Application of Method II yielded D_0 and w fields identical to those given by Method I. For Method II, the N_0 has been found to be greater than that for Method I. The retrieved melting band attenuation at the shorter wavelength was similar to that for Method I.

The retrieval occasionally yielded unphysical negative melting band attenuations at the longer wavelength. This has been attributed to an overestimate of the water vapor attenuation by our assumption of a saturated atmosphere. Summary results have been presented in the form of profiles of horizontal averages of observed and retrieved quantities. The averaged vertical air velocity is noteworthy. The magnitudes and vertical variation of the velocity are remarkably similar to what has been reported in the literature for area-averaged vertical velocity in extensive stratiform rain measured by the VAD method. The averaged profile of rainfall rate, N_0 and D_0 has shown evidence of drop breakup below the melting band and evaporation in the lower levels in the region of downdrafts. The potential ability to retrieve the parameters of the RSD, the vertical air velocity, and the water vapor distribution as functions of the height is exciting because it offers the possibility of direct calculation of profiles of evaporation and, therefore, latent cooling in the atmosphere using microphysical principles.

Acknowledgements

We thank Ed Zenker and Paul Racette for their engineering support. This work is supported by Dr. R. Kakar of NASA Headquarters under NASA's Precipitation Measurement Mission grant 621-15-46. The data were collected during the CRYSTAL-FACE campaign that was funded by the NASA Radiation Science Program. The work of Ramesh Srivastava is supported by NSF grant ATM 0314049.

Appendix A
List of Symbols

$A\ (\alpha)$: Attenuation factor, number (dB)

$a_i,\ b_i\ h_i$: Fit coefficients for D_0, $\partial\xi$, and k_{mm}/Z_{cm}, $i = 0,1,2,3$

$c_{(\,)}$: Unit Conversion Factor for Quantity $(\ )$

D_0: Medium Volume Diameter

$k\ (\kappa)$: Two-Way Specific Attenuation / Length, $\left(\text{dB km}^{-1}\right)$

N_0: Intercept of Raindrop Size Distribution

$N(D)$: Raindrop Size Distribution

V_t: Terminal Fall Speed

$\bar{V}$: Mean Doppler Velocity

w: Vertical Air Velocity

$Z:(\xi)$ Reflectivity, $\text{mm}^6\,m^{-3}$ (dBZ)

$\partial(\ ) = (\ )_{cm} - (\ )_{mm}$

Λ: Slope Parameter

σ: Cross-section

Subscripts

$BACK$: Back-Scattering

cm: 3.2 cm Wavelength

EXT: Extinction

MB: Melting Band

mm: 3.2 mm Wavelength

p: Precipitation

Superscripts

(gas): Gas, Water Vapor

(m): Measured

(ppt): Precipitation

Reference

Atlas, D., R. C. Srivastava and R. S. Sekhon, 1973: Doppler radar characteristics of precipitation at vertical incidence. *Rev. Geophys., Space Phy*, **11**, 1-35.

Battan, L., 1973: *Radar Observation of the Atmosphere*. University of Chicago Press, 324 pp.

Bellon, A., I. Zawadski, and F. Frederic, 1997: Measurements of melting layer attenuation at X-bnad frequency. Radio Science, 32, 943-954.

Eccles, P.J., and E. A. Muller, 1971: X-band attenuation and liquid water content estimation by dual-wavelength radar. *J. Appl. Meteor.*, **10**, 1252-1259.

Foote, G. B., and P. S. du Toit, 1969: Terminal velocity of raindrops aloft. *J. Appl. Meteor.*, **8**, 249-253.

Heymsfield, G.M., S.W. Bidwell, I.J.Caylor, S. Ameen, S. Nicholson, W. Boncyk, L. Miller, D. Vandemark, P.E. Racette, and L.R. Dodd,1996: The EDOP radar system on the high-altitude NASA ER-2 aircraft. *J. Atmos. Oceanic Technol.*, **13**, 795-809.

Houze, R. A., 1993: Cloud Dynamics, Chapter 9, Academic Press, 570 pp.

Iguchi, T. Kozu, R. Meneghini, J. Awaka, and K. Okamoto, 2000: Rain-profiling algorithm for the TRMM precipitation radar. *J. Appl. Meteor.*, **39**, 2038-2052.

Li, L., G. M. Heymsfield, P. E. Racette, L. Tian and E. Zenker. 2004: A 94-GHz Cloud Radar System on a NASA High-Altitude ER-2 Aircraft. *J. Atmo. Oceanic Technol.*, **21**, 1378–1388.

Marshall, J. S., and W. M. K. Palmer, 1948: the distribution of raindrops with size. *J. Meteor.*, **5**, 165-166.

Meneghini, R., S. W. Bidwell, R. Rincon, G. M. Heymsfield, and L. Liao, 2003: Differential-frequency Doppler weather radar: Theory and experiment. *Radio Sci.* 38, 1-10.

Mishchenko, I. M., D. T. Larry, A. A. Lacis, 2003: *Scattering, Absorption and Emission of Light by Small Particles*, Cambridge University Press, 462 pp.

Pruppacher , H. R., and Pitter, R. L., 1971: A semi-empirical determination of the shape of cloud and raindrops. *J. Atmos. Sci*, **28**, 86-94.

Roger, R. R., 1964: An extension of the Z-R relation for Doppler Radar. Proc., 11th Radar Conf. Boston, Amer. Meteor. Soc., 158-161.

Tokay, A., and D. A. Short, 1995: Evidence from tropical raindrop spectra of the origin of rain from stratiform versus convective clouds. *J. Appl. Meteor.*, **35**, 355-371.

Uijlenhoet, R., M. Steiner, and J. A. Smith, 2003: Variability of raindrop size distribution in a squall line and implications for radar rainfall estimate. *J. Hydrol.*, **4**, 43-61.

Ulaby, F. T., R. K. Moore, and A. K. Fung, 1982*: Microwave Remote Sensing: Active and Passive.* Vol. 1. Addison-Wesley, 607 pp.

Ulbrich, C. W., 1983: Natural variations in the analytical form of the raindrop-size distribution., *J. Climate Appl. Meteorol*, **22**, 1764-1775.

Waldvogel, A., 1974: The N_0 jump of raindrop spectra, *J. Atmos. Sci.*, **31**, 1067-1078.

LIST OF TABLE

Table 1. Characteristics of the radars

	EDOP	CRS
Wavelength (cm)	3.115	0.32
Peak power (kW)	7.6	1.7
Beam width (°)	2.9 (circular)	0.6 (cross-track), 0.8(along track)
Pulse width (μs)	0.5	1.0
PRF (kHz)	4.444	4, 5 (dual PRF)
Antenna gain (dB)	36.1 (nadir), 35.5 (forward)	46.4
Range gate(m)	37.5	37.5

Table 2. Refractive Index for temperatures of 5, 15, 25 C.

lambda(cm)	Temp(C)	cmr	cmi	K2
3.2	5.	7.566178	-2.652102	0.929839
3.2	15.	7.996637	-2.196946	0.928027
3.2	25	8.204579	-1.760490	0.925601
0.3184	5.	2.937504	-1.512247	0.723597
0.3184	15.	3.210343	-1.789401	0.787677
0.3184	25.	3.509437	-2.061058	0.834507

Table 3. Fitting coefficient of polynomials for D_0, $\xi_{cm} - \xi_{mm}$, and k_{mm}/Z_{cm}, $0.01 \text{ mm} < D_0 < 1.18 \text{ mm}$.

	T °C	$i=0$	$i=1$	$i=2$	$i=3$
a_i	5	1.5553e+00	-1.2189e-02	4.2473e-05	-5.4137e-08
b_i	5	1.1192e+02	-9.4368e-01	3.8068e-03	-5.3191e-06
h_i	5	-3.4896e-03	4.3816e-05	-1.8029e-07	2.4544e-10
a_i	15	1.4457e+00	-1.0759e-02	3.6361e-05	-4.5433e-08
b_i	15	1.0280e+02	-8.2215e-01	3.2727e-03	-4.5403e-06
h_i	15	-3.0819e-03	3.8333e-05	-1.5610e-07	2.1030e-10
a_i	25	1.4308e+00	-1.0527e-02	3.5169e-05	-4.3388e-08
b_i	25	1.0447e+02	-8.3573e-01	3.2919e-03	-4.5067e-06
h_i	25	-3.2502e-03	4.0007e-05	-1.6104e-07	2.1407e-10

LIST OF FIGURES

Figure 11. Profiles of the quantities in the schema shown in Fig. 10 for the same selected horizontal distance as of Fig. 9.

Figure 12. Averaged profiles: a) Measured reflectivity at cm ($\xi_{cm}^{(m)}$) and mm ($\xi_{mm}^{(m)}$) wavelength. ξ_{cm}, shown by the triangle is the reflectivity after corrected for melting band attenuation at cm wavelength. b) Measured Doppler velocity at mm and cm wavelength, and retrieved vertical air speed, w, which is scaled. c) Retrieved D_0 and N_0 (circle). The triangle is the N_0 after corrected for melting band attenuation at cm-wavelength. d) Rainfall rate and rainwater content. The circle is the quantities before corrected for melting band attenuation and the triangle is the quantities after corrected for melting band attenuation. e) Averaged estimated water vapor attenuation (solid). The dotted line is the water vapor attenuation calculated from the sounding for a saturated atmosphere.

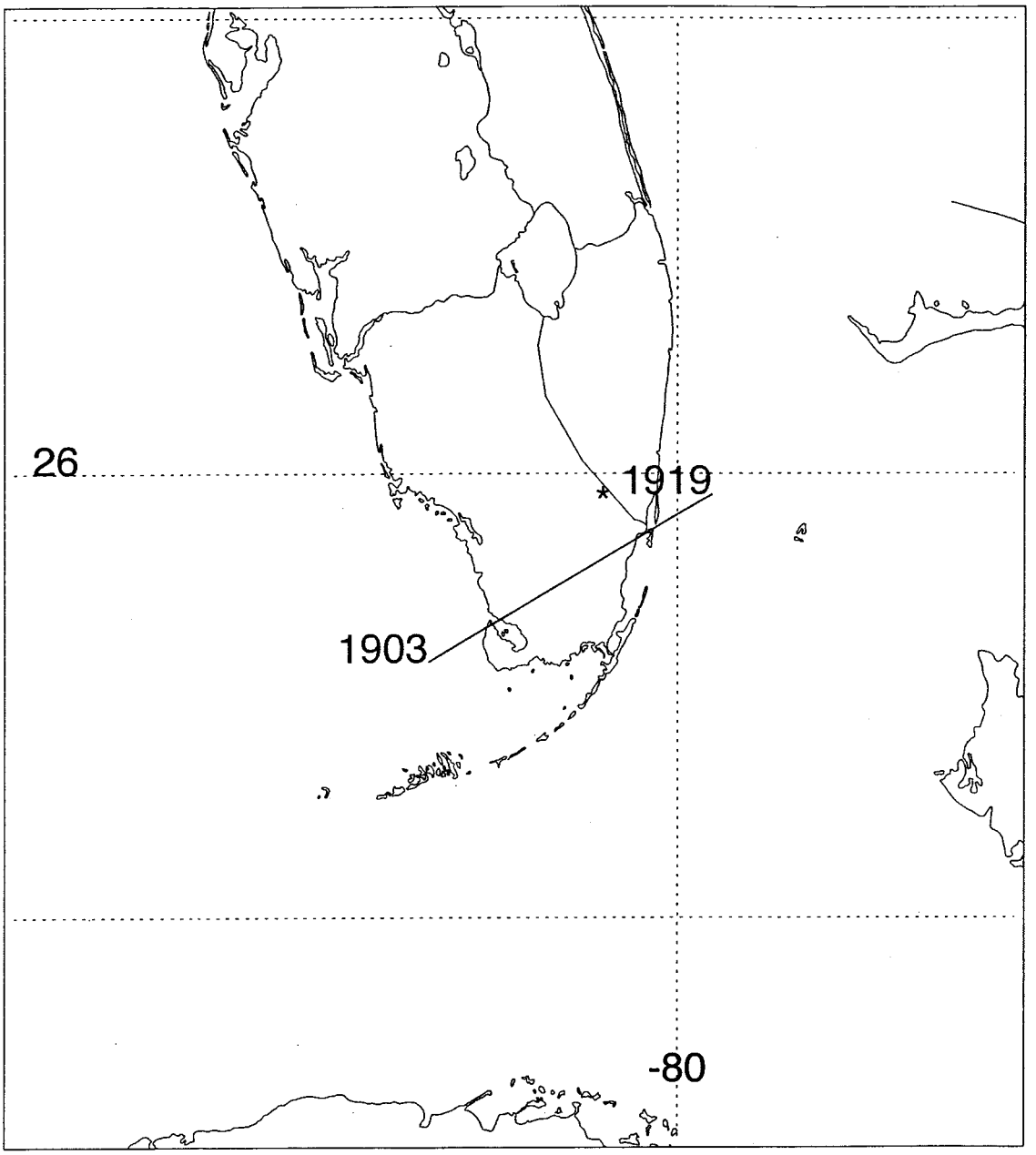

Figure 1 Flight track on 11 July, 1903-1919. The stratiform cloud is at the end of the flight line on the east coast of Florida. Location of the sounding in Fig. 3 marked by "*".

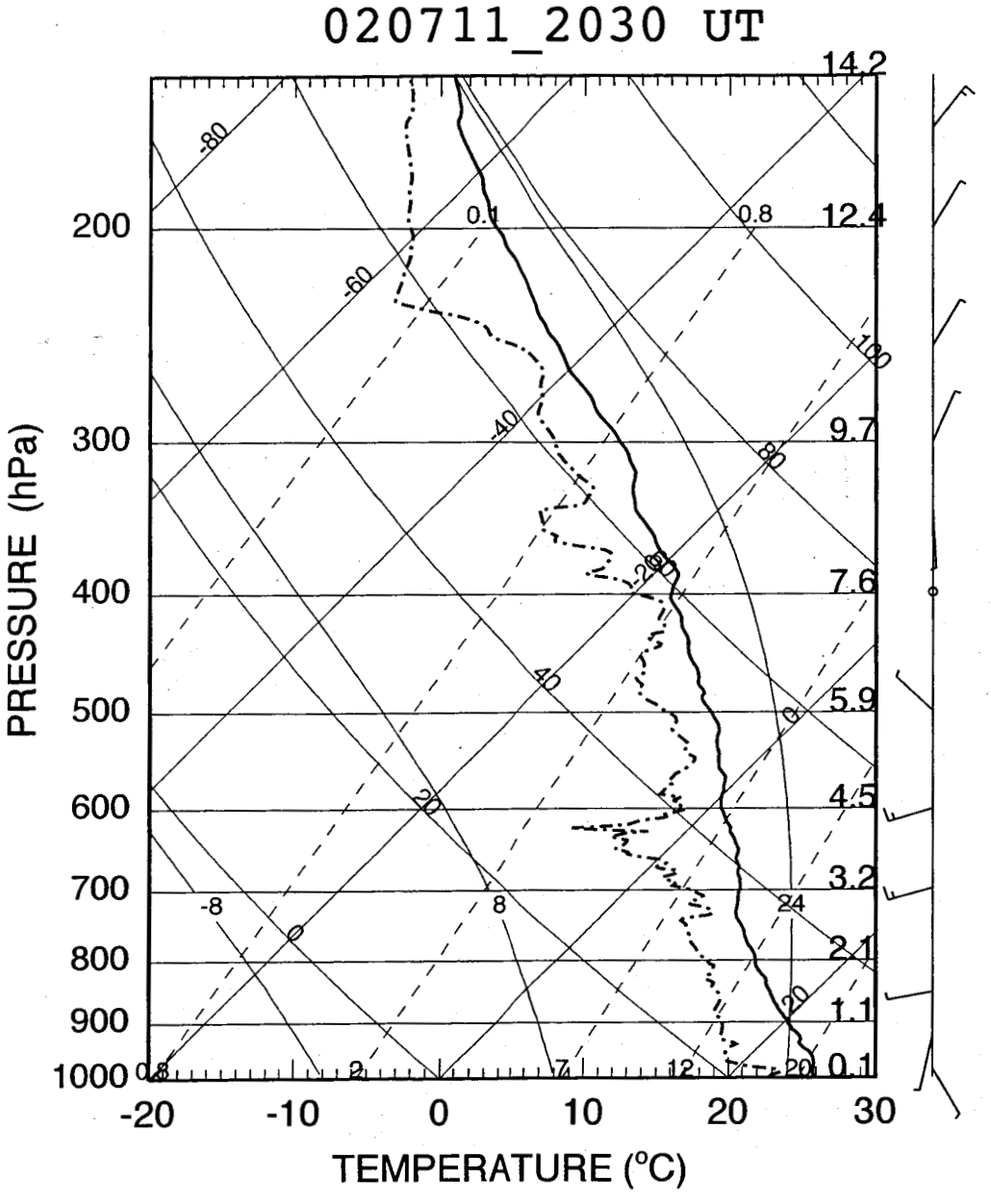

Figure 2. Sounding at Miami at 2030 UTC, July 11, 2002.

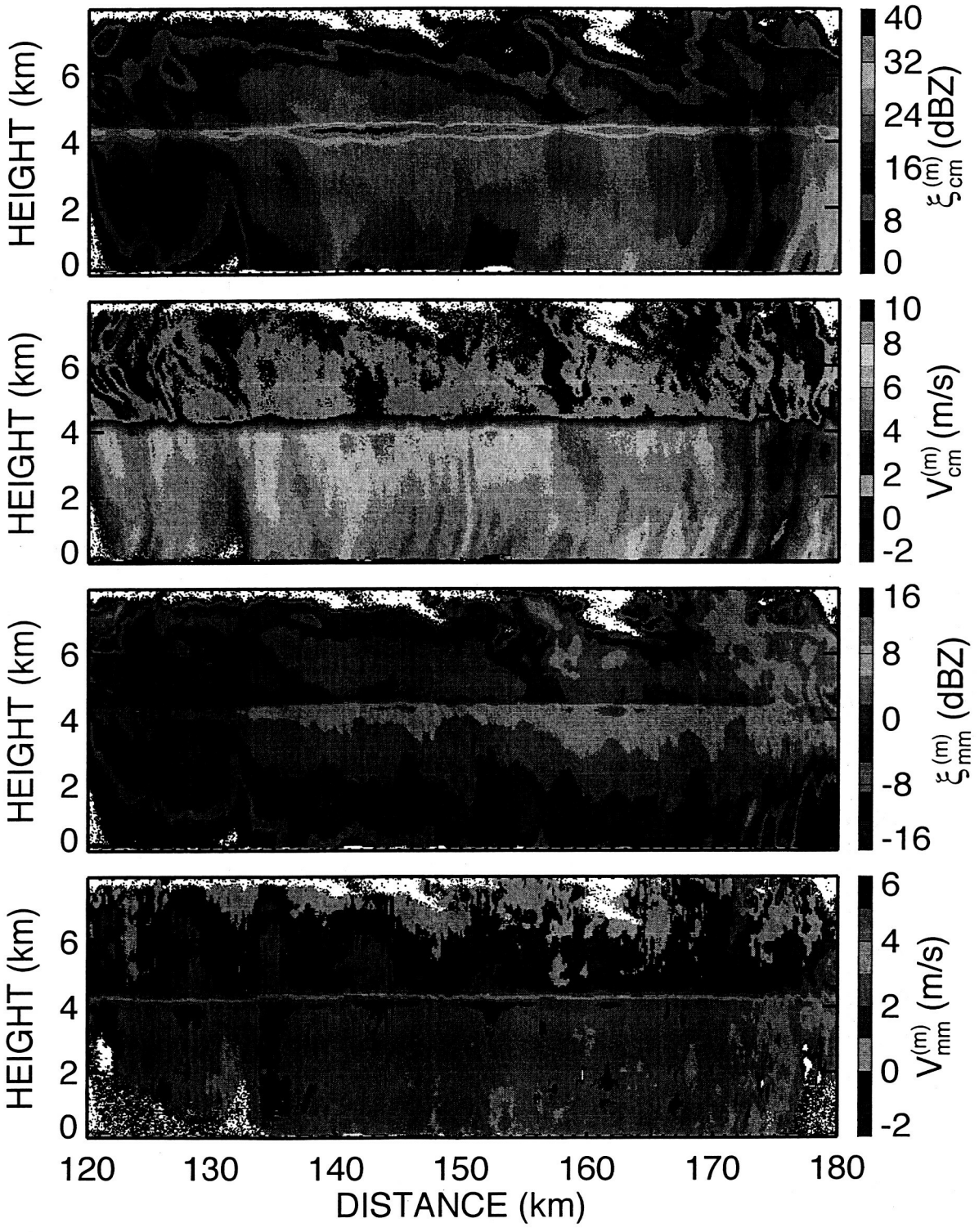

Figure 3. a) $\xi_{cm}^{(m)}$, b) $\overline{V}_{cm}^{(m)}$, c) $\xi_{mm}^{(m)}$, and d) $\overline{V}_{mm}^{(m)}$ on July 11, 2002 during 1909-1911 UT.

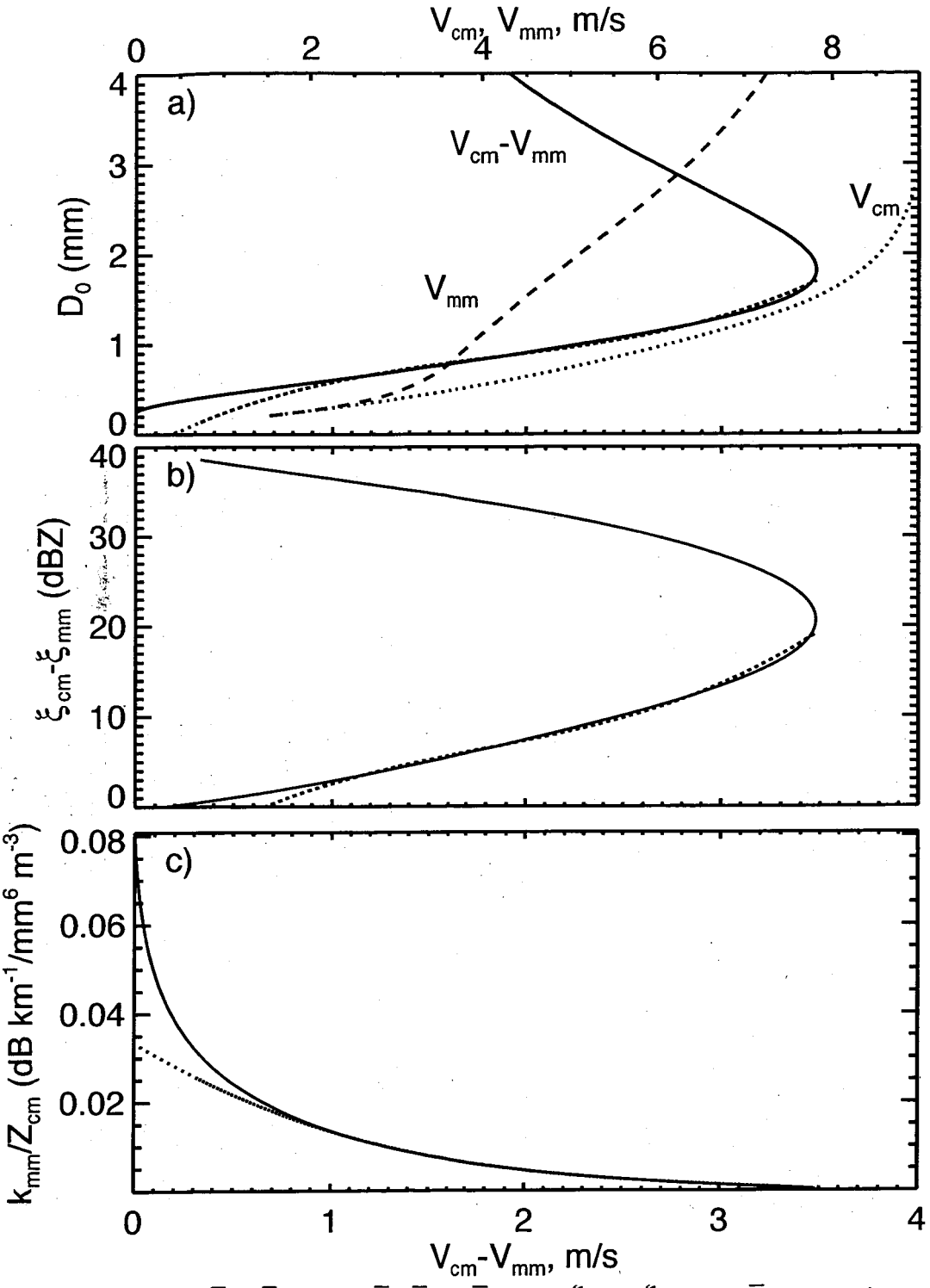

Figure 4. (a) D_0 vs. $\bar{V}_{cm}$, $\bar{V}_{mm}$, and $\partial\bar{V}=\bar{V}_{cm}-\bar{V}_{mm}$; b) $\xi_{cm}-\xi_{mm}$ vs. $\partial\bar{V}$; c) κ_{mm}/Z_{cm} vs. $\partial\bar{V}$. The dotted line is the polynomial fit.

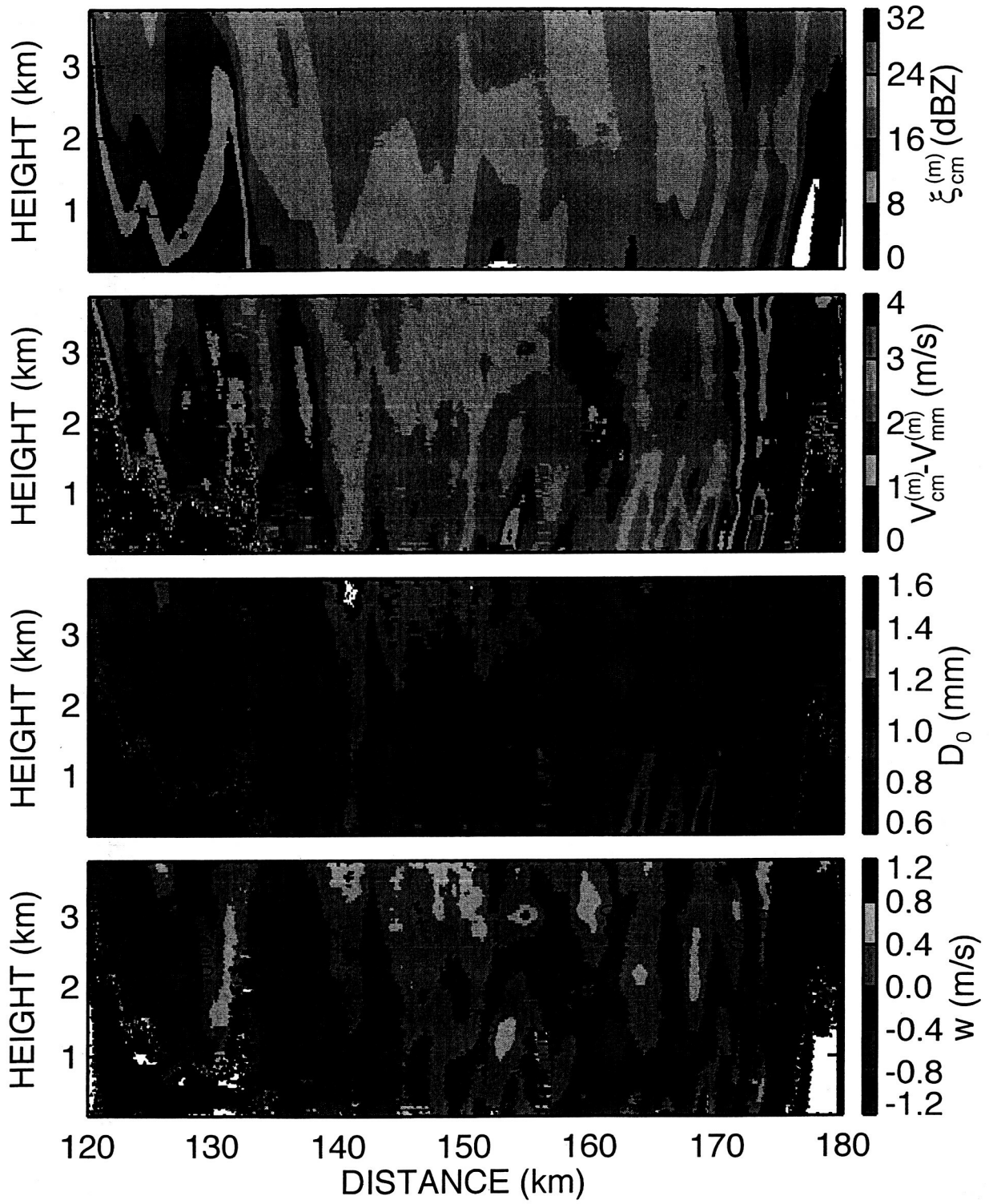

Figure 5. a) $\xi_{cm}^{(m)}$, b) $\partial\overline{V}$, c) retrieved D_0 from $\partial\overline{V}$, and d) w, retrieved vertical air motion.

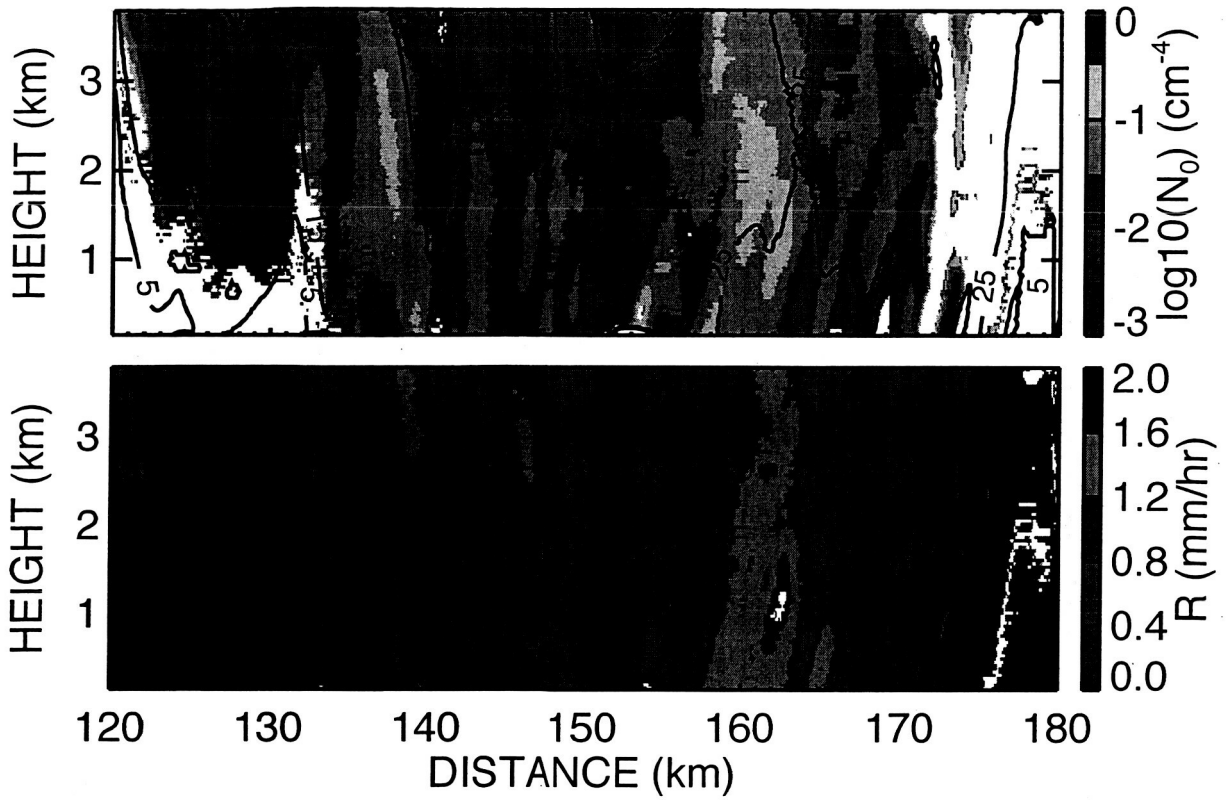

Figure 6. a) Retrieved N_0 ; b) Rainfall rate, R, calculated from the retrieved N_0 and D_0.

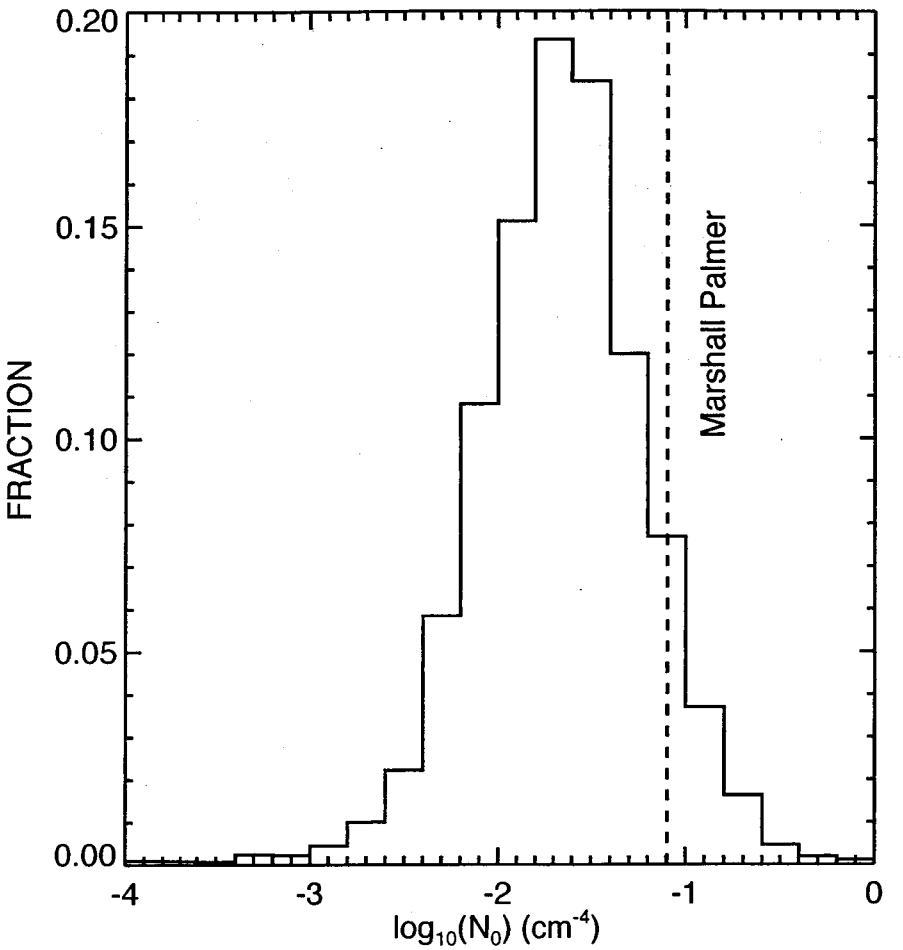

Figure 7a. Histogram of retrieved N_0 value. $N_0 = 0.08\ \mathrm{cm}^{-4}$ (dash line) is for Mashall Palmer distribution.

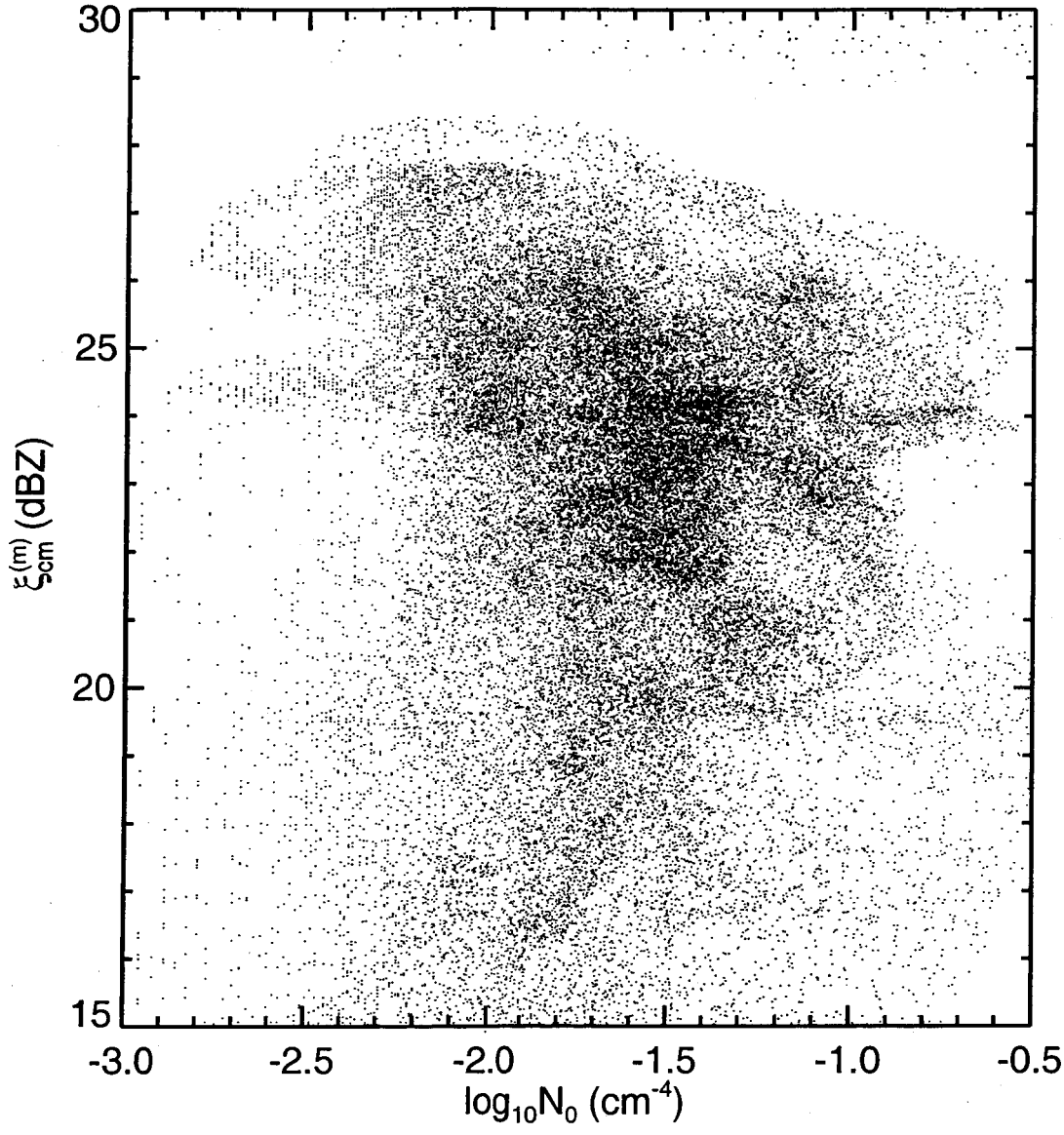

Figure 7b. Scatter plot of $\xi_{cm}^{(m)}$ vs. retrieved N_0.

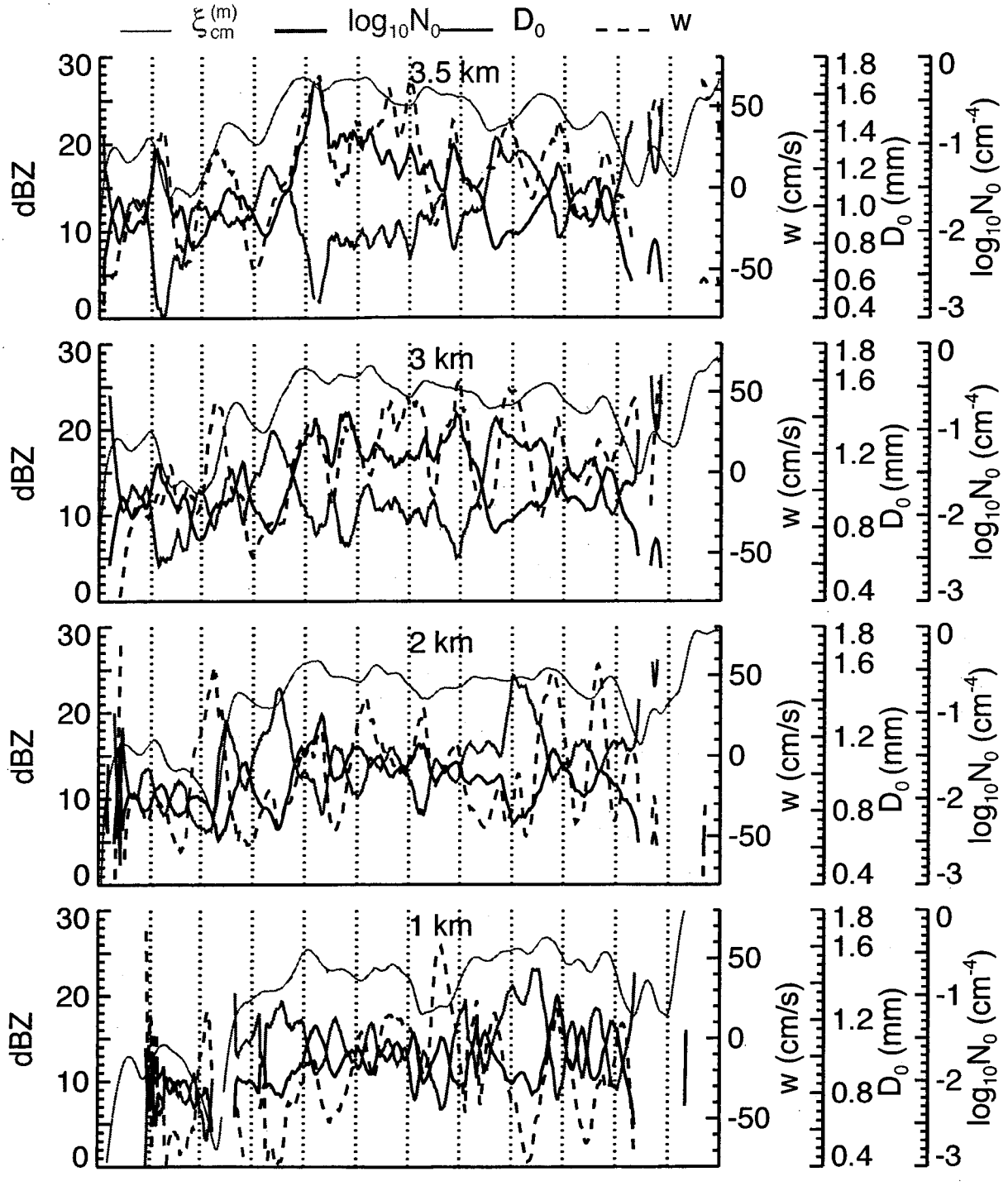

Figure 7c. Plot of $\xi_{cm}^{(m)}$, N_0, D_0, and w along the flight line for selected heights of 1, 2, 3, and 3.5 km.

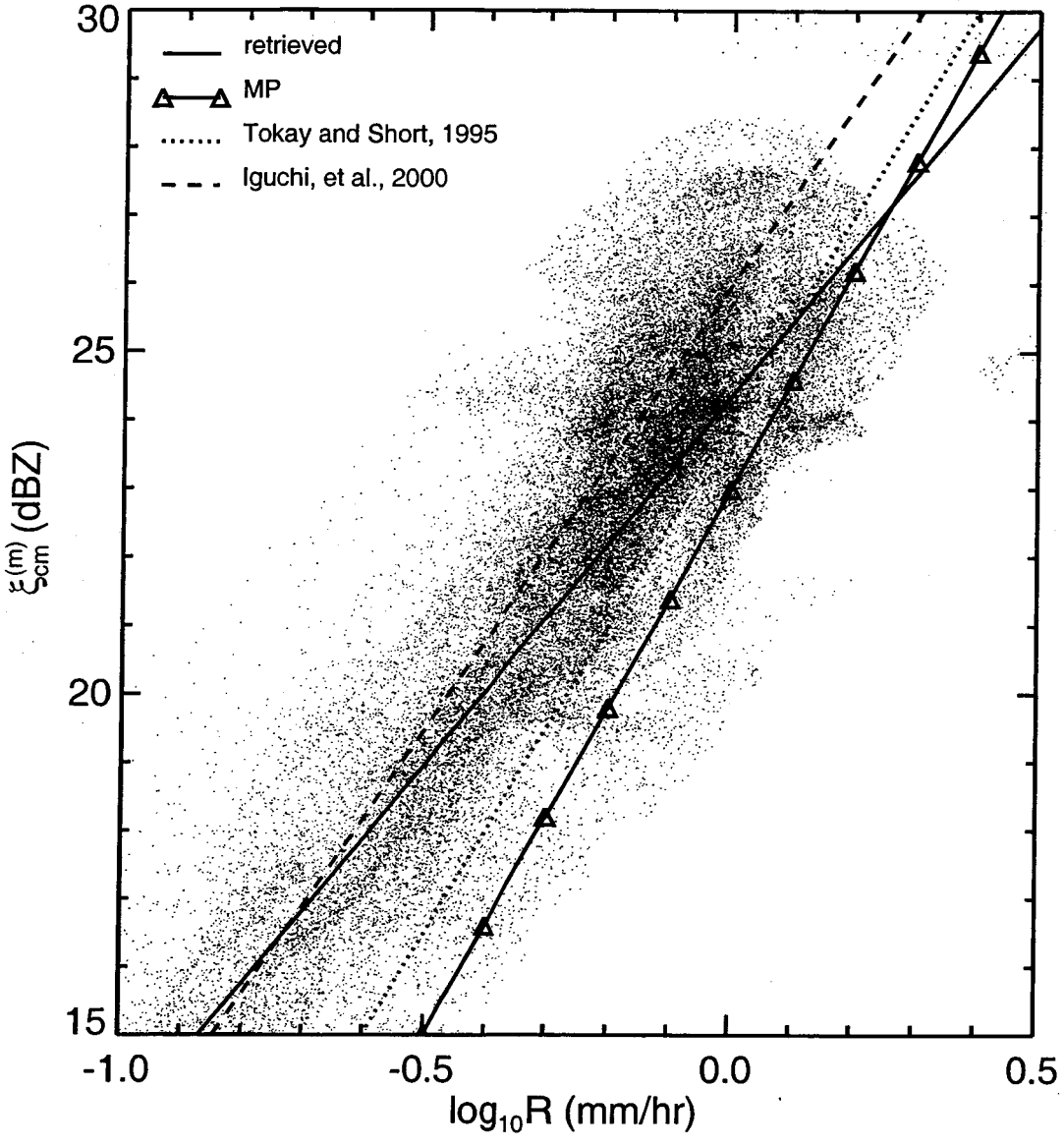

Fig. 7d Scatter plot of retrieved $\xi_{cm}^{(m)}$ against N_0 and corresponding Z-R relation. Three other Z-R relations for stratiform rain from Marshall-Palmer (MP), Darwin, Australia (Tokay and Short, 1995), and that used by TRMM precipitation radar (Iguchi, et al. 2000) are also shown.

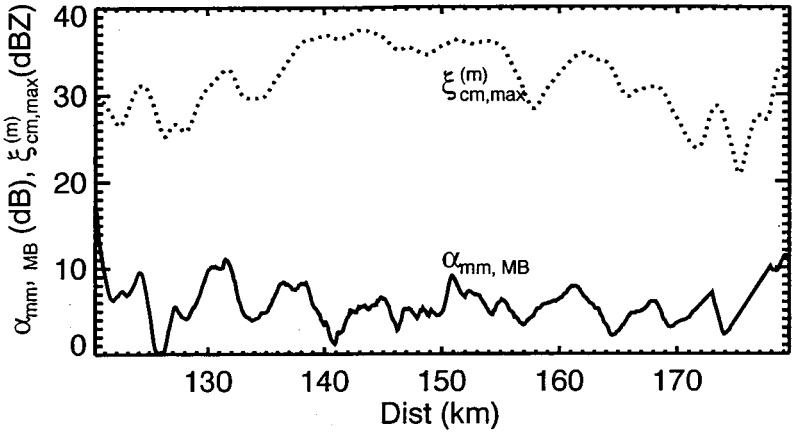

Figure 8a – mm wave attenuation from top of cloud to r0

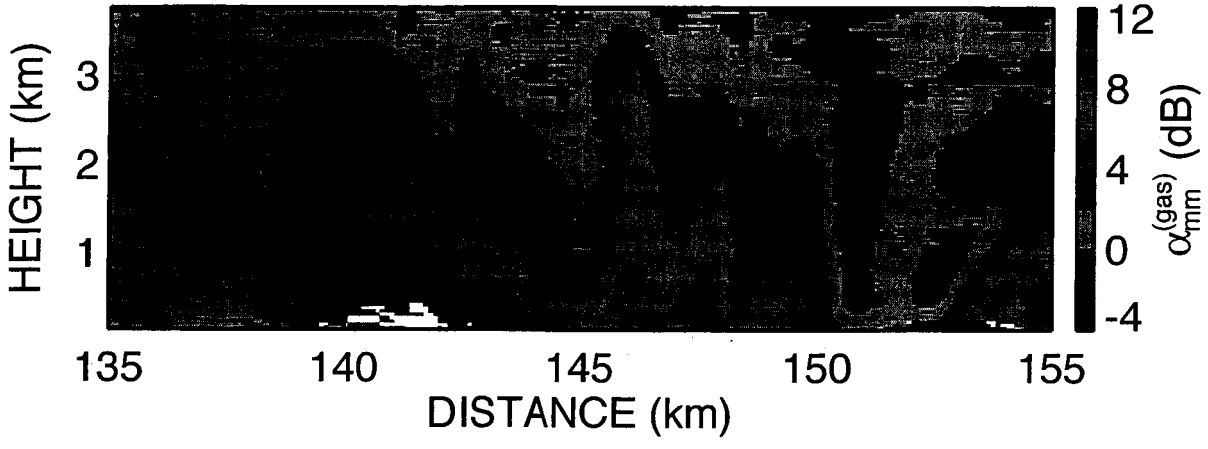

Figure 8b Same as fig8a except the distance is limited to between 135 and 155 km.

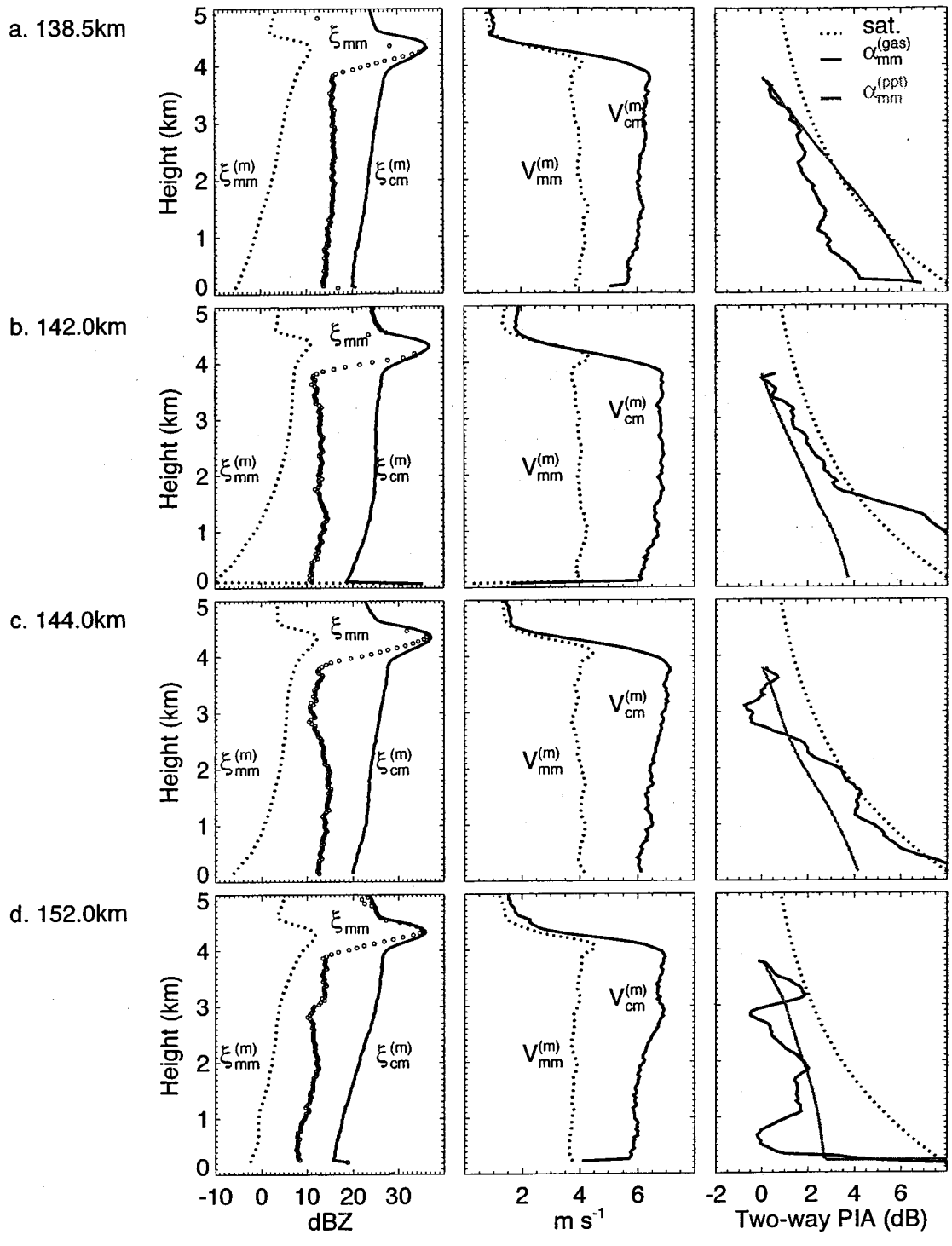

Figure 9. Profiles for selected horizontal distance of 138.5, 142.0, 144, and 152 km. Left: $\xi_{cm}^{(m)}$, $\xi_{mm}^{(m)}$, and ξ_{mm}; Middle: $V_{cm}^{(m)}$ and $V_{mm}^{(m)}$; Right: Retrieved water vapor attenuation $\alpha_{mm}^{(gas)}$ (black solid) and rain attenuation $\alpha_{mm}^{(ppt)}$(gray solid). The dotted line is the water vapor attenuation estimated from the sounding shown in Fig. 2, assuming a saturated atmosphere.

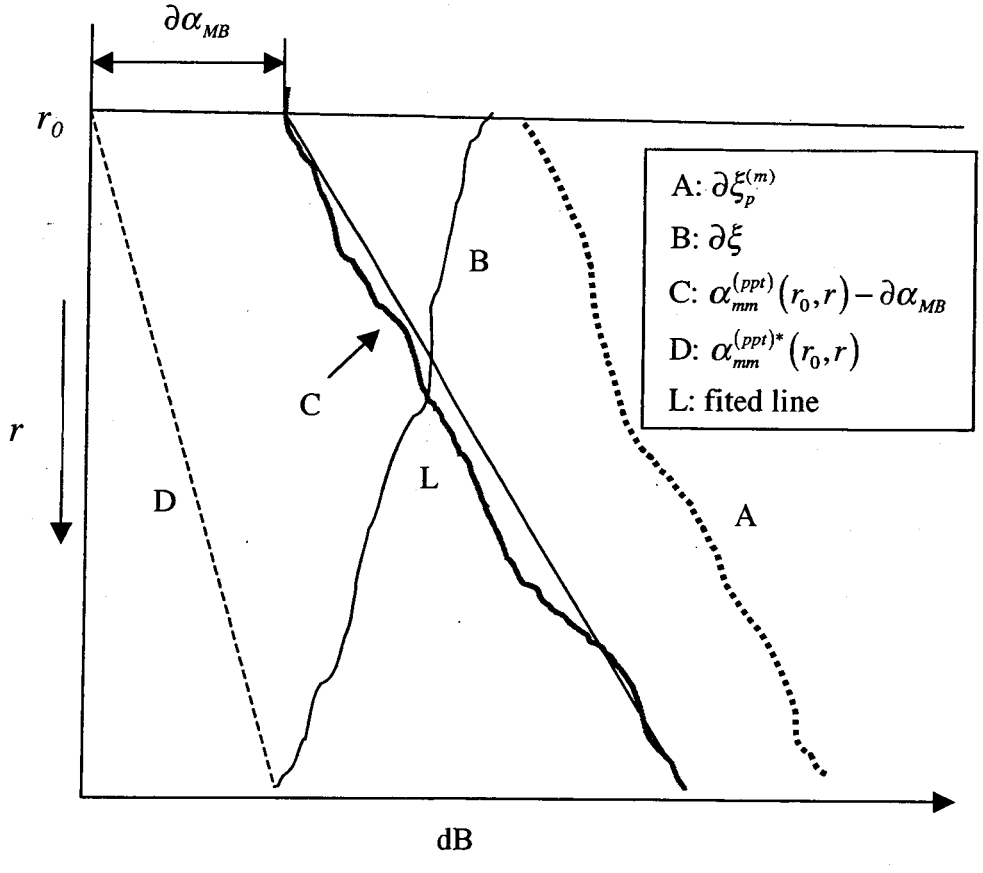

Figure 10. The schematic to illustrate method II.

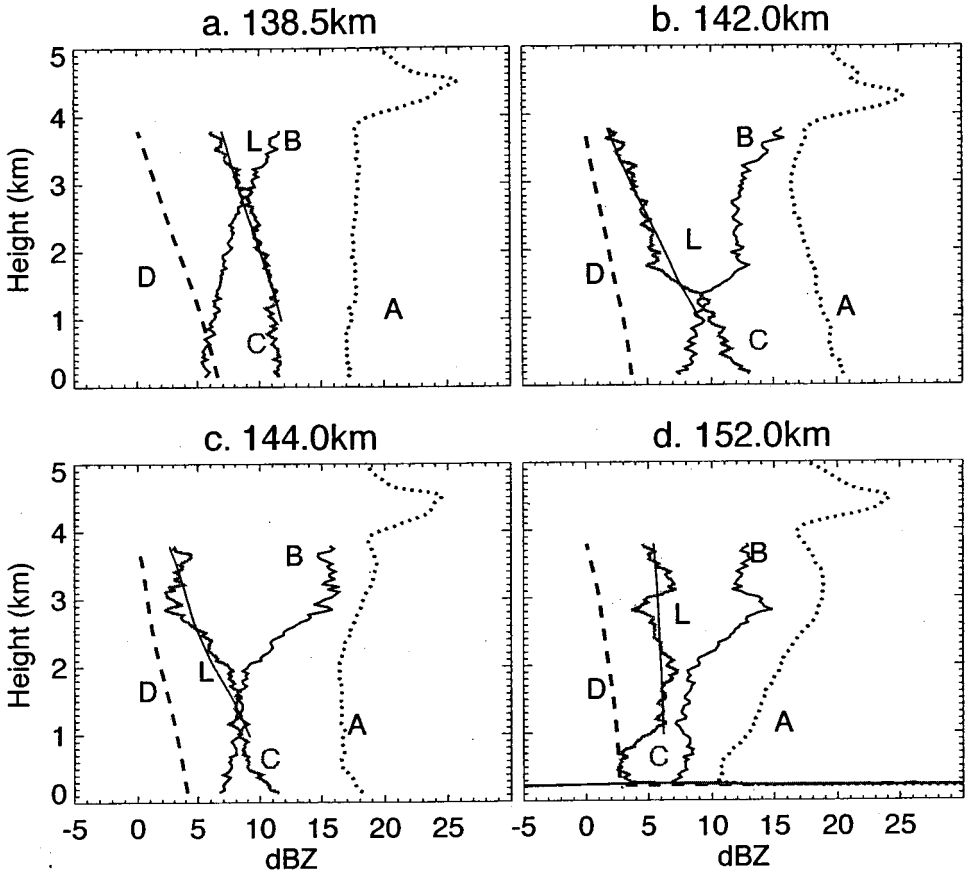

Figure 11. Profiles of the quantities in the schema shown in Fig. 10 for the same selected horizontal distance as of Fig. 9.

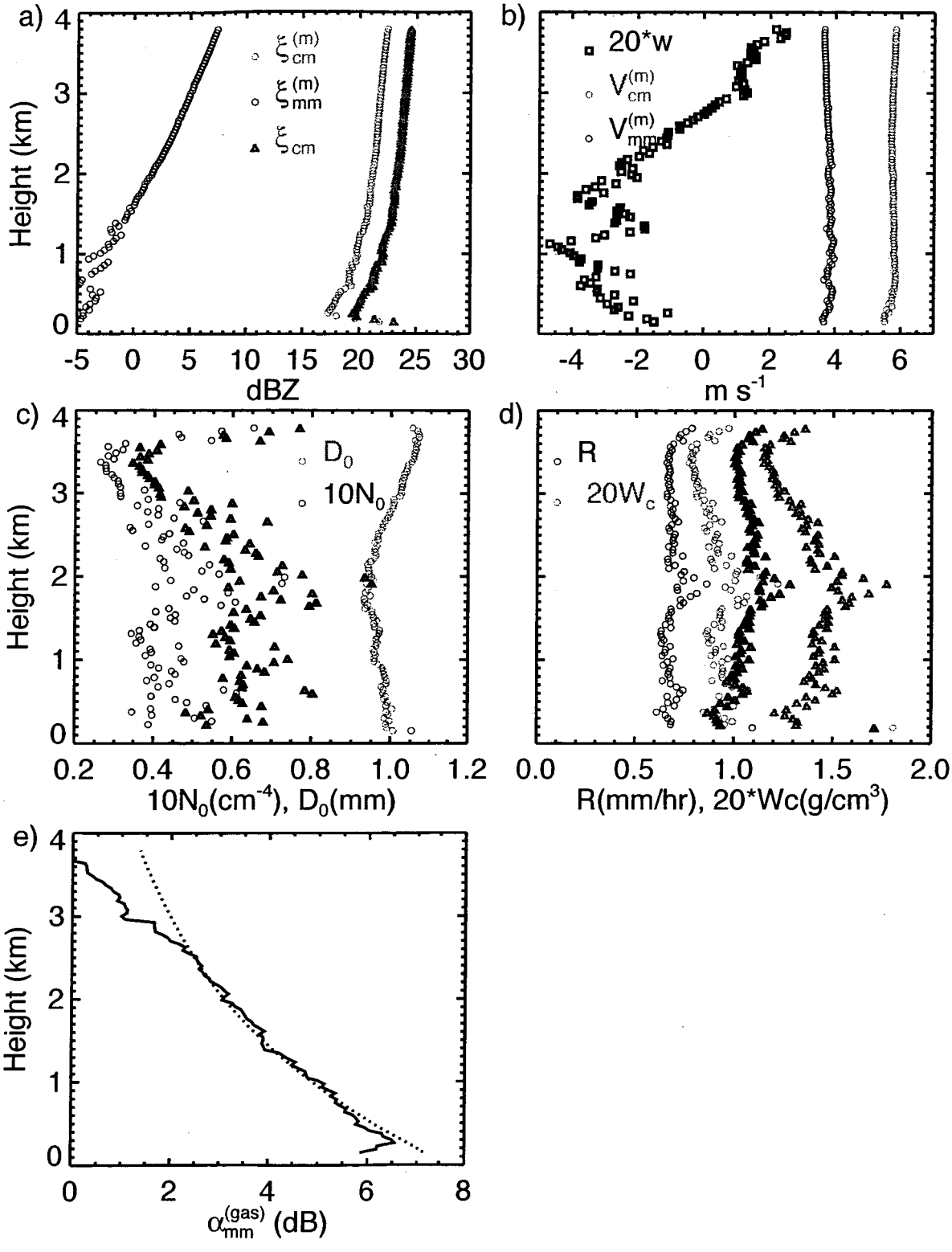

Figure 12. Averaged profiles: a) Measured reflectivity at cm ($\xi_{cm}^{(m)}$) and mm ($\xi_{mm}^{(m)}$) wavelength. ξ_{cm}, shown by the triangle is the reflectivity after corrected for melting band attenuation at cm wavelength. b) Measured Doppler velocity at mm and cm wavelength, and retrieved vertical air

speed, w, which is scaled. c) Retrieved D_0 and N_0 (circle). The triangle is the N_0 after corrected for melting band attenuation at cm-wavelength. d) Rainfall rate and rainwater content. The circle is the quantities before corrected for melting band attenuation and the triangle is the quantities after corrected for melting band attenuation. e) Averaged estimated water vapor attenuation (solid). The dotted line is the water vapor attenuation calculated from the sounding for a saturated atmosphere.